Review

Check for updates

Self-terminated electrodeposition of Pt group metal: principles, synthetic strategies, and applications

Hyunki Kim[1], Seokjin Hong[1], Junbeom Bang[1], Yeji Jun[1], Seonghyun Choe[1], Soo Young Kim[2,*] iD **, Sang Hyun Ahn[1,*]** iD

[1]School of Chemical Engineering and Material Science, Chung-Ang University, Seoul 06974, Republic of Korea.
[2]Department of Materials Science and Engineering, Korea University, Seoul 02841, Republic of Korea.

***Correspondence to:** Prof. Sang Hyun Ahn, School of Chemical Engineering and Material Science, Chung-Ang University, 84, Heukseok-ro, Dongjak-gu, Seoul 06974, Republic of Korea. E-mail: shahn@cau.ac.kr; Prof. Soo Young Kim, Department of Materials Science and Engineering, Korea University, 145, Anam-ro, Seongbuk-gu, Seoul 02841, Republic of Korea. E-mail: sooyoungkim@korea.ac.kr

Abstract

Hydrogen, characterized by its carbon-neutral attributes and high energy density, is gaining momentum as a promising energy source. Platinum group metal (PGM) catalysts have emerged as pivotal components in water electrolysis and fuel cell technologies. However, their constrained availability and high cost impede the advancement of energy conversion systems. To address these challenges, various strategies have been explored within the realm of PGM catalysts. Particularly noteworthy are catalysts that exhibit an overlayer structure, offering exceptional catalyst utilization efficiency, bimetallic synergies, and strain-induced enhancements. Self-terminated electrodeposition (SED) stands out as a technique that enables precise atomic layer electrodeposition within an aqueous electrolyte environment. It allows meticulous control of metal loading quantities and surface coverage while operating at low temperatures and without the need for vacuum conditions. Catalysts with tailored properties achieved through SED exhibit distinct electrochemical reactivity compared to bulk catalysts, showcasing exceptional electrocatalytic activity, particularly in terms of mass and specific activity. This comprehensive review provides insights into the SED phenomenon, elucidates methodologies for fabricating PGM electrocatalysts using SED, and highlights their applications in water electrolysis and fuel cells.

Keywords: Self-terminated electrodeposition, Pt group metal catalyst, atomic layer deposition, fuel cell, water electrolysis

INTRODUCTION

Hydrogen plays a central role in the chemical industry, functioning as one of the world's largest producers and consumers. It serves as a crucial component in the manufacturing of a wide range of high-volume chemicals, including ammonia, urea, and methanol, and in applications such as refineries, the metal and glass industry, and the food industry[1,2]. Furthermore, in response to the increasing global energy demand[3-6], hydrogen has become a focal point of intrigue as a versatile energy carrier, lauded for its carbon-free attributes and substantial energy content of 140 MJ kg^{-1}[7]. Nevertheless, at present, steam reforming of natural gas contributes to over 50% of hydrogen generation[8], leading to unavoidable carbon emissions. In conjunction with renewable energy sources, water electrolysis presents a promising avenue for generating pure hydrogen without carbon footprints[8-11].

The hydrogen obtained by water electrolysis can be used to produce a large amount of clean electricity in fuel cells. Furthermore, in order to address the challenges of hydrogen storage, transportation, cost, and safety[12-14], various fuel cell technologies have adopted liquid alternatives, such as ethanol, methanol, and formic acid[15]. These technologies, applied across a wide range of applications, align with their respective advantages and disadvantages, making significant contributions to the development of a hydrogen-based society[15]. In particular, methanol-based fuel cells offer the advantages of high energy density and low operating temperatures, making them suitable for ultra-compact portable devices[16,17]. In contrast, formic acid has gained attention for its capacity to be produced from CO_2[18,19].

To materialize the concept of a hydrogen-based society, the development of highly efficient water electrolyzers and fuel cell systems remains pivotal. Elevating the efficiency of energy conversion systems necessitates the utilization of highly active catalysts. Consequently, in recent years, there has been growing interest in developing cost-effective and highly active electrocatalysts. In particular, owing to their vacant *d* electron configurations, transition metal-based electrocatalysts have emerged as promising candidates in various energy conversion technologies[20,21]. The presence of *d* electrons enables them to directly participate in redox reactions, facilitating the exchange of electrons and the formation of chemical bonds with reactants[20,21]. Among the transition metal, Pt group metal (PGM) catalysts show remarkable activity in water electrolysis[22,23] and various fuel cell systems such as hydrogen-[24,25], methanol-[16,26], formic acid-[18,27], and ammonia-fuel cells[28]. Nonetheless, their elevated cost and limited availability impede the advancement of energy conversion systems. To address this issue, a wide range of approaches have been investigated for PGM catalysts, including the incorporation of non-PGM metals, organic materials, supporting materials, and nanostructure engineering[29-32].

Among these options, the catalyst with an overlayer (core-shell) structure stands out as one of the most promising candidates due to its exceptional catalyst utilization efficiency. Additionally, a bimetallic effect can arise from lattice strain between the catalyst overlayer and substrate. By engineering this lattice strain, the d-band center of the PGM catalyst can be tuned, facilitating the weakening or strengthening of intermediates in electrochemical reactions[33,34]. This offers a compelling avenue for enhancing catalytic performance.

Several synthesis methods are available for the fabrication of overlayer catalysts, including core-shell structures through gas- or solution-phase synthesis[35,36]. While gas-phase synthesis offers precise control over composition and nano-scale thickness, it necessitates high temperatures, vacuum conditions, and expensive equipment such as chemical vapor deposition, physical vapor deposition, and sputtering[37-39]. Solution-phase synthesis with the chemical reduction method for producing core-shell catalysts requires the use of capping agents and potentially toxic solvents. Moreover, to apply particle-shaped catalysts to real devices, a process involving the mixing of ionomers and subsequent spray or coating is necessary.

By contrast, electrochemical methods were performed in aqueous electrolytes under moderate conditions[21,40]. Additionally, a benefit of this approach is the direct applicability of electrode-formed deposits to devices without the need for additional processes[40-42]. The surface-limited redox reaction (SLRR) method primarily involves underpotential deposition (UPD) and subsequent galvanic displacement, enabling the fabrication of overlayer-structured catalysts, especially with noble metal-based materials. However, this two-step process requires the exchange of electrolytes, and it poses a substantial risk of sacrificial ion residues accumulating on the surface of the catalyst, consequently initiating the discontinuous growth of the layer[43]. The reversible nature of UPD reactions introduces challenges in managing deposition procedures, especially when aiming for sub-nanometer scale films.

On the other hand, self-terminated electrodeposition (SED) facilitates atomic layer electrodeposition in aqueous electrolytes[44-46]. Accurate management of metal loading quantities and coverage is attainable at low temperatures, all without the need for vacuum environments or capping agents. When the suitable electrodeposition potential is applied, the reduction of metal is promptly halted as the metal is reduced on the surface due to the saturated hydrogen or hydroxide coverage[44-46]. This phenomenon is referred to as self-terminated or self-limited electrodeposition[44]. The passivated surface can be re-activated by shifting the potential to a positive value, allowing for the oxidation of limiting agents (e.g., hydrogen and hydroxide layers) to take place[44,46].

Applying these principles, continuous cyclic voltammetry (CV) or pulsing methods enable the metal electrodeposition at the atomic layer level, ranging from a few-atom and monolayer levels to layer-by-layer structures in Table 1[44,46-72]. It allows for the swift production of multilayer electrodes, which is a suitable approach for making film substrates required in fundamental research on the electrochemical reactions of specific metals[69,73]. Furthermore, it has been demonstrated to be highly successful in a wide range of research domains, including applications in pH measurement and electrocatalysis [Table 1]. In particular, this method offers the capability of depositing alloyed layers comprising not only monovalent metals but also bimetallic combinations, thereby providing a catalytic avenue for diverse applications across various fields. This review provides a comprehensive overview of the fundamental aspects of SED, the influencing factors on SED, and the characterization of electrodes fabricated through SED. Moreover, it highlights various applications of electrodes produced via SED as catalysts in water electrolysis and various fuel cell systems.

PRINCIPLES AND SYNTHETIC APPROACHES FOR SED OF PGM
PGM varieties exhibiting the SED phenomenon and their fundamental mechanisms
The SED has been reported for not only PGM but also Fe group metals. However, the primary objective of this study is to offer an in-depth examination of SED within the context of PGM. Table 1 compiles a comprehensive summary of PGM catalyst types produced through SED, encompassing the substrates employed, electrodeposition conditions, material properties, and their respective applications[44,46-72].

The SED phenomenon for the PGM was first reported by Moffat group[44]. Pt electrodeposition was performed on Au-coated Si (100) wafers in 3 mM Pt K_2PtCl_4 and 0.5 M NaCl, with pH values ranging between 2.5 and 4. While conducting a negative scan in linear scan voltammetry (LSV), the authors tracked the Pt loading mass using current features and the electrochemical quartz crystal microbalance (EQCM). In Figure 1A, the LSV indicates Pt deposition initiating at 0.25 V *vs.* sodium-saturated calomel reference electrode (V_{SSCE}). A significant current peak occurs around -0.32 V_{SSCE} due to diffusion-limited $PtCl_4^{2-}$

Table 1. PGM catalyst types produced through SED, encompassing the substrates employed, electrodeposition conditions, material properties, and their respective applications

Catalyst	Substrate	Electrolyte	Electrodeposition method	Thickness /nm	Coverage /%	Loading /μg cm^{-2}	Application	Ref.
Pt	Au-coated quartz crystal electrode	3 mM K_2PtCl_4 + 0.5 M NaCl, pH 4.0	1~10 pulses at room temp: 0.4 V_{SSCE} for 2 s, -0.8 V_{SSCE} for 5 s, 0.4 V_{SSCE} for 30 s	0.21~0.25	10~85	0.486	-	[44]
Pt	Ni/Au electrode	3 mM K_2PtCl_4 + 0.5 M NaCl, pH 4.0	1~5 pulses at room temp: -0.8 V_{SSCE} for 0~2,000 s	0.23~0.5	0~60	1	HER, HOR	[46]
Pt	Au wafer	3 mM K_2PtCl_4 + 0.5 M NaCl, pH 3.5	1~10 pulses at room temp: -0.8 V_{SSCE} for 5 s, 0.4 V_{SSCE} for 30 s	0.2~1.1	60~75	0.364	MOR, FAOR	[47]
Ir	Au film, Pt film, Au RDE, Pt RDE	3 mM K_3IrCl_6 + 0.5 M Na_2SO_4, pH 1.5, 4.0, 6.5	1~10 pulses at 40-70 °C: 0 V_{SSCE} for 2 s, -0.45 V_{SSCE} for 2 s	0.1~3.2	30~50	-	HER, HOR, ORR, OER	[48]
Pt	WC	3 mM K_2PtCl_4 + 0.5 M NaCl, pH 4.0	0~20 CV at room temp: 0.8~-0.45 V_{SCE}, 50 mV s^{-1}	-	1.04~15.8	0.036~0.835	HER, HOR	[49]
Pt	C/CP	10 mM K_2PtCl_4 + 0.5 M NaCl, pH 4.0	1~50 pulses at room temp: 0.4 V_{SCE} for 2 s, -0.9 V_{SCE} for 5-100 s, 0.4 V_{SCE} for 2 s	-	-	-	HER	[50]
Ir	Au/CP	3 mM K_3IrCl_6 + 0.5 M Na_2SO_4, pH 4.0	1~50 pulses at 70 °C: -1.2 V_{MSE} for 10 s, -0.3 V_{MSE} for 2 s	-	8.1~73.5	1.53~13.35	OER	[51]
Pt	Au dendrite/CP	3 mM K_2PtCl_4 + 0.5 M NaCl, pH 4.0	1 pulse at room temp: 0.4 V_{SCE} for 5 s, -0.9 V_{SCE} for 5 s, 0.4 V_{SCE} for 5 s	-	-	9.6	FAOR	[52]
Pt	Au/CP	3 mM K_2PtCl_4 + 0.5 M NaCl, pH 4.0	1~10 pulses at room temp: 0.4 V_{SCE} for 5 s, -0.9 V_{SCE} for 5 s	-	45~88	5	FAOR	[53]
Pt	CP	3 mM K_2PtCl_4 + 0.5 M NaCl, pH 4.0	1~500 pulses at room temp: 0.4 V_{SCE} for 2 s, -0.9 V_{SCE} for 10 s, 0.4 V_{SCE} for 3 s	-	-	0.03~271	HER	[54]
Pt	Pt/C-a	3 mM K_2PtCl_4 + 0.5 M NaCl, pH 4.0	1~100 pulses at room temp: 0.4 V_{SCE} for 2 s, 0.9 V_{SCE} for 10 s, 0.4 V_{SCE} for 3 s	-	-	50	HOR	[55]
Pt	TiN	3 mM K_2PtCl_4 + 0.5 M NaCl, pH 4.0	1~40 pulses at room temp: -0.75 V_{SCE} for 20 s, 0.2 V_{SCE} for 15 s	-	-	0.93	MOR	[56]
Pt	Au NF/Ni foam	3 mM K_2PtCl_4 + 0.5 M NaCl, pH 4.0	1~10 pulses at room temp: -0.4 V_{SCE} for 5 s, 0 V_{SCE} for 5 s	0.25	-	0.55	HER	[57]
Pt	Au/Ni/CF	3 mM K_2PtCl_4 + 0.5 M NaCl, pH 4.0	1 pulse at room temp: 0.39 V_{RHE} for 5 s, -0.51 V_{RHE} for 5 s	0.27	-	0.553	HER	[58]
Pt	Au/Ni	3 mM K_2PtCl_4 + 0.5 M NaCl, pH 4.0	1~3 pulse at room temp: 0.10 V_{SCE} for 5 s, -0.72 V_{SCE} for 5 s	0.3	-	0.555	HER	[59]

Pt	Au film	5~30 mM K_2PtCl_4 + 0.1-1.0 M of NaCl, KClO$_4$, NaBr or NaI	1 pulse at room temp: -0.8 $V_{Ag/AgCl}$ for 200 s	-	-	-	-	[60]
Pt	Dendritic Au rod	3 mM K_2PtCl_4 + 0.5 M NaCl, pH 4.0	1-30 pulses at room temp: -0.75 $V_{Ag/AgCl}$ for 10 s, 0.4 $V_{Ag/AgCl}$ for 30 s	-	30~100	-	FAOR	[61]
Pt	NPG Au	3 mM K_2PtCl_4 + 0.5 M NaCl, pH 4.0	1-150 pulses at room temp: 0.4 $V_{Ag/AgCl}$ for 2 s, -0.8 $V_{Ag/AgCl}$ for 10~3,000 s, 0.4 $V_{Ag/AgCl}$ for 30 s	-	-	-	pH sensors	[62]
Pt	Dendritic Au rod	3 mM K_2PtCl_4 + 0.5 M NaCl	1-15 pulses at room temp: -0.75 $V_{Ag/AgCl}$ for 10 s, 0.4 $V_{Ag/AgCl}$ for 30 s	-	-	-	MOR	[63]
Pt	NPG Au	3 mM K_2PtCl_4 + 0.5 M NaCl, pH 4.0	50 pulses at room temp: 0.40 V, -0.80 V	-	-	-	OER	[64]
Ir	Ti$_2$AlC	1-3 mM K_3IrCl_6 + 0.5 M Na$_2$SO$_4$, pH 6.2	1-5 CV at 70 °C: 0.44~-0.60 V_{NHE}, 5 mV s^{-1}	4.5~255	-	11-572	HER	[65]
Ir	Ti$_2$AlC	1-3 mM K_3IrCl_6 + 0.5 M Na$_2$SO$_4$, pH 6.2	1 LSV at 70 °C: 0.15 V_{NHE}~-0.55 V_{NHE}, 5 mV s^{-1}	-	-	2.995	HER	[66]
Ir	Ti$_2$AlC	3 mM K_3IrCl_6 + 0.5 M Na$_2$SO$_4$ + 0.5 M H$_2$SO$_4$, pH 6.2	1-3 CV at 70 °C: 0.2 V_{SCE}~-0.86 V_{SCE}, scan: 5 mV s^{-1}	58~85	-	-	OER	[67]
Pt	(Nb-Ti)$_2$AlC	2-3 mM K_2PtCl_4 + 0.5 M NaCl, pH 4.0	1 LSV at room temp: 0.00 V_{SCE} ~ -0.80 or -0.90 V_{SCE}, 2 mV s^{-1}	-	-	2.98-29.82	ORR	[68]
Pt	Au film	3 mM K_2PtCl_4 + 0.5 M NaCl, pH 4.0	Pulse at room temp: 0.4 V_{SCE} for 2 s, -0.8 V_{SCE} for 15 s, 0.4 V_{SCE} for 30 s	-	-	-	ORR	[69]
Pt	Au dendrimer-encapsulated nanoparticles	3 mM K_2PtCl_4 + 0.5 M NaCl, pH 4.0	1-10 pulses at room temp: -0.014 $V_{HgHg2SO4}$ for 30 s, -1.2 $V_{HgHg2SO4}$ for 1 s	-	85	-	-	[70]
Pt	Au$_{poly}$, TiO$_x$/Ti	3 mM K_2PtCl_4 + 0.5 M NaCl, pH 4.2	1 pulse at room temp: Mass-transfer controlled proton-reduction region for 30 s (Au$_{poly}$) or for 150 s (TiO$_x$/Ti)	-	-	-	ORR	[71]
Pt	Au dendrimer-encapsulated nanoparticles	3 mM K_2PtCl_4 + 0.5 M NaCl, pH 4.0	1-10 pulse at room temp: 0.86 V_{RHE} for 30 s, -0.34 V_{RHE} for 1 s, 0.86 V_{RHE} for 1 s	0.6	57~97	-	FAOR	[72]

reduction. After -0.5 V_{SSCE}, there was a sharp current drop, hitting a minimum near -0.7 V_{SSCE}, and then, the current increased again due to hydrogen evolution. The authors confirmed that the sharp current drop below -0.5 V_{SSCE} corresponds to a complete cessation of metal deposition through the EQCM result.
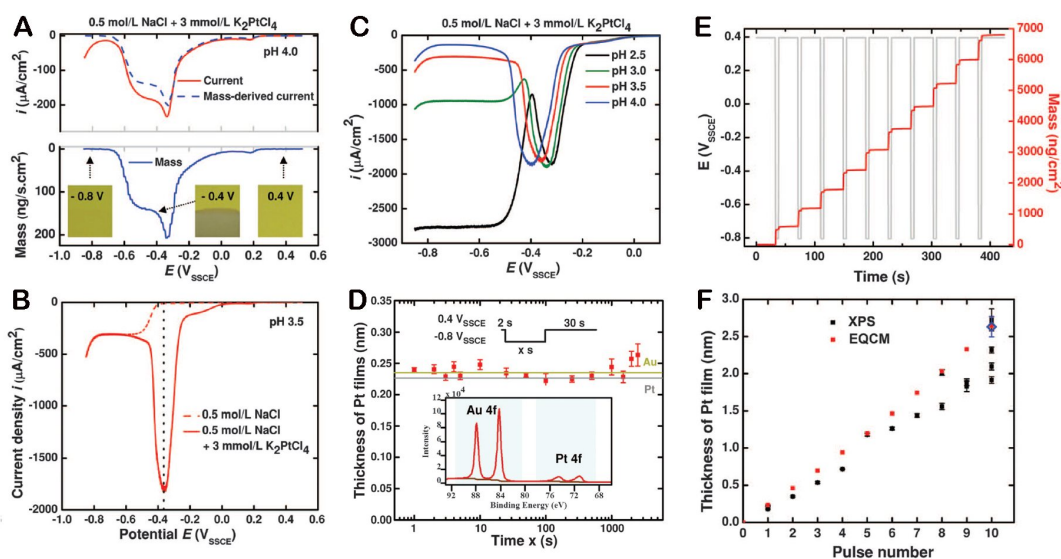
Figure 1. (A) Gravimetric and (B and C) voltammetric assessments of Pt deposition from 3 mM Pt K_2PtCl_4 and 0.5 M NaCl using either a static EQCM or an RDE (400 rpm). The insets are optical images of Pt films grown on Au-coated Si(100) wafers for 500 s at the indicated potentials. (D) Evolution of Pt film thickness, derived from XPS analysis, in relation to deposition time at -0.8 V_{SSCE} on Au-coated Si(100) wafers, obtained from a pH 4 solution. (E) Mass change accompanying each potential pulse. (F) Pt thickness obtained by XPS and EQCM results as a function of Pt deposition pulse number. This figure is quoted with permission from Liu *et al.*[44].

This remarkable self-termination of Pt deposition was also exhibited when the Pt deposition was performed on an Au rotating disk electrode (RDE) with a rotation speed of 400 revolutions per minute (rpm) [Figure 1B]. Additionally, when performing LSV on a Pt RDE within a Pt precursor-free electrolyte and varying the pH from 2.5 to 4.0, a pH-dependent and H_{UPD}-correlated rapid current increase below -0.2 V_{SSCE} became apparent. Conversely, when adjusting pH on an Au RDE to investigate Pt deposition through LSV, the Pt deposition rate increased with H_{UPD} coverage, reaching a pH-independent peak value [Figure 1C]. As potentials became more negative, the deposition rate rapidly declined, merging with the current driven solely by proton reduction within 0.1 V of its peak, indicating full suppression of Pt deposition. CV results revealed reversible Pt deposition passivation, in line with the H_{UPD} onset potential. From these results, the authors suggested that the self-termination of the Pt deposition arose from perturbation of the double-layer structure that accompanies H_{ads} saturation of the Pt surface while diffusion-limited proton reduction continues unabated.

The thickness and loading mass of Pt on Au were compared by varying the deposition time and the number of Pt pulses [Figure 1D-F]. After fixing the deposition potential at -0.8 V_{SSCE}, X-ray photoelectron spectroscopy (XPS) confirmed the Pt thickness to be around 0.21 and 0.25 nm, approaching the monolayer level, with a time range from 1 to 1,000 s [Figure 1D, F]. *In situ* scanning tunneling microscopy (STM) was employed to observe the morphology of the Pt overlayer, as depicted in Figure 2, revealing a fractional surface coverage of Pt close to 0.85.

Figure 3A depicted the CV feature of Ir deposition on an Au RDE in a pH 4 electrolyte. It was indicated that at room temperature, the Ir^{3+} d^6 complex remained inert, making it challenging to confirm Ir^{3+} reduction. However, at a temperature above 40 °C, the current could be observed. Similar to the study of Pt SED, self-termination occurred with the initiation of hydrogen production, followed by diffusion-limited proton reduction below -0.85 V_{SSE} (SSE: saturated K_2SO_4 filled Hg_2SO_4/HgO electrode) in Figure 3A and B. As shown in Figure 3B, as the pH decreases, the onset potential of Ir^{3+} reduction decreases while the peak
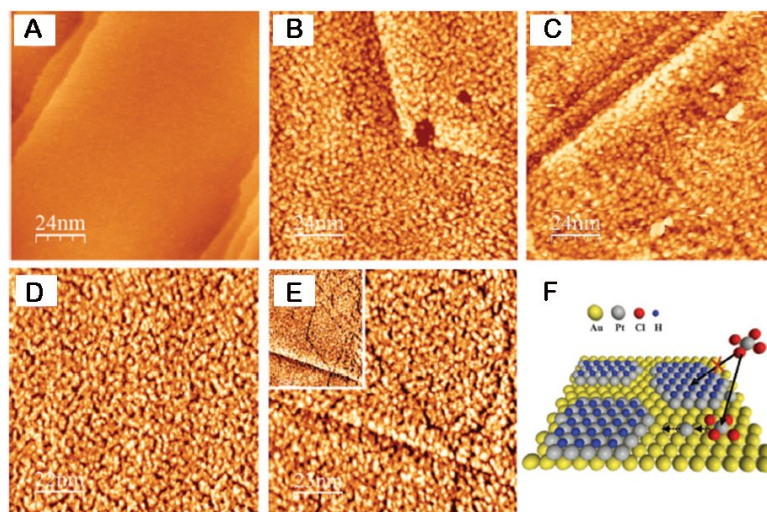
Figure 2. (A) STM images depicting a characteristic Au(111) surface adorned with monoatomic steps. Images of 2D Pt layers formed after (B) 5 s and (C) 500 s of deposition at -0.8 V_{SSCE}. (D) High-contrast visual representation of the morphology of a 2D Pt layer on Au(111). (E) Linear defects within a Pt layer, arising from the elevation of the reconstructed Au substrate. Inset showcases a lower-magnification view. (F) A schematic depiction illustrating the Pt SED on Au(111). This figure is quoted with permission from Liu *et al.*[44].
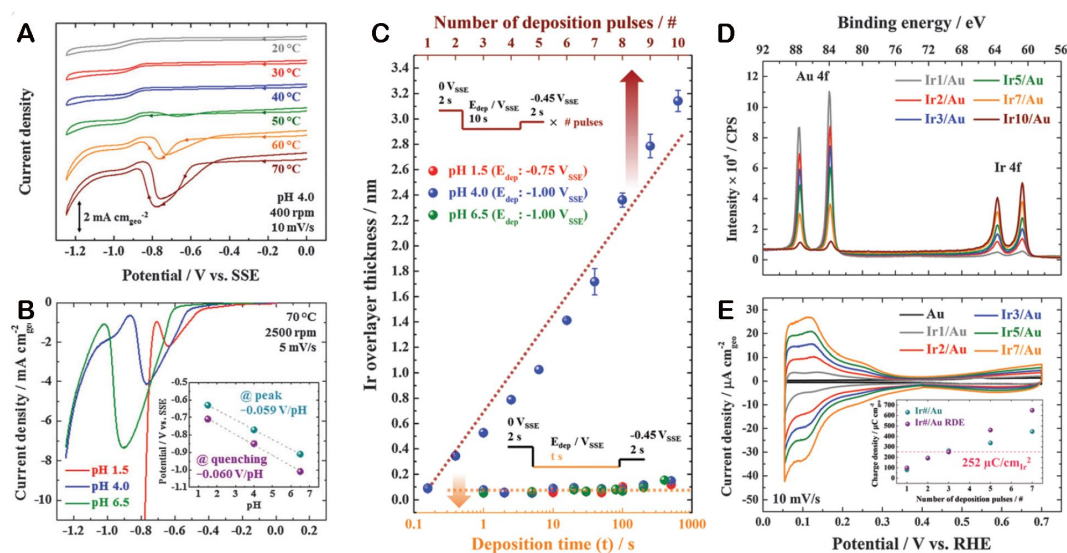

Figure 3. (A) Ir deposition investigation on Au RDE in 3 mM K_3IrCl_6 and 0.5 M Na_2SO_4 from a pH 4 electrolyte. (B) LSV curve of Ir SED, depending on pH of electrolytes. (C) XPS-derived Ir thickness on Au-seeded Si wafer, accounting for varying electrolyte pH levels and deposition times. (D) Evident Au 4f and Ir 4f spectra and (E) characteristic CV features in 0.5 M H_2SO_4, modulated by the number of Ir deposition pulses. This figure is quoted with permission from Ahn *et al.*[48].

deposition current rises. For low Ir^{3+} concentrations and when electrode rotation rates are slow, the peak current demonstrates a consistent relationship with the Ir^{3+} flux. However, as rotation rates surpass 1,600 rpm, the peak current reaches saturation, revealing the prevalence of surface processes. At room temperature, octahedral $IrCl_6^{3-}$ exhibits limited reactivity in water exchange. Nevertheless, at 70 °C, the transform of $IrCl_6^{3-}$ into $[IrCl_5H_2O]^{2-}$ and $[IrCl_4(H_2O)_2]^-$ was verified through UV-visible absorption spectroscopy[74,75]. Despite this, the authors confirmed through CV that the fundamental attributes of Ir SED deposition remained relatively unchanged even after the aging of the Ir^{3+} precursors.

XPS analysis was conducted to examine the amount of Ir deposited on Au-seeded Si wafers [Figure 3C and D]. A single Ir SED pulse results in an Ir thickness of 0.085 ± 0.028 nm, employing a uniform Ir overlayer model. This implies that the single Ir pulse forms Ir clusters or islands, covering 25% to 50% of the surface in Figure 3C. Furthermore, similar to Pt, the Ir coverage demonstrated independence not only from deposition time but also from pH. By configuring pulses along with the potential of -0.45 V_{SSE}, which is capable of re-activating a quenched surface, an increase in the number of pulses showed that Ir thickness could be monotonically adjusted. This trend was evident from the measured charge density in the H_{UPD} region [Figure 3E]. When employing a single pulse, the fractional Ir surface coverage was approximately 0.32, and then, after three pulses, it reached the level of a monolayer. Thus, using the SED method, monolayer-level Pt and Ir can be obtained on Au film substrates under low-temperature and ambient-pressure conditions in a matter of seconds. Furthermore, it has been confirmed that the thickness of the overlayer can be incrementally increased, even from levels below 0.21 nm.

SED on porous Au substrate structures

After the initial findings involving Pt and Ir overlayers on thin Au substrates through SED[44,48], further investigations have emerged. These subsequent studies have delved into the utilization of dendritic Au structures and Au substrates with porous gas diffusion layer architectures. These innovative approaches have been explored for SED applications, particularly as electrodes in water electrolysis and fuel cell systems[51,53,59,60,61,66,72].

A Pt layer on a dendritic Au rod structure (DAR) substrate was prepared by electrodeposition in an electrolyte containing 36 mM Au(I) ions complexed with sulfite anions[76-78]. The DAR substrate was prepared through electrodeposition in an electrolyte containing 36 mM Au(I) ions complexed with sulfite anions. The Pt SED was performed on DAR by repetitive potential pulse using a solution of 3 mM K_2PtCl_4 and 0.5 M NaCl (pH 4), with pulses of -0.75 V for 10 s followed by 0.4 V for 30 s. By increasing the pulse cycles (*n*) from 1 to 30, the Pt-to-Au electrochemical surface area (ECSA) ratio of DAR@Pt(*n*) was compared, enabling the analysis of surface composition. For DAR@Pt(1), a Pt coverage of 30% corresponding to submonolayer Pt loading was confirmed. As the number of cycles increased, the Pt coverage monotonically increased, reaching 100% at 15 cycles, thus achieving a monolayer of the Pt coverage.

Li *et al.* reported a comprehensive monolayer Pt coating technique employing a layer-by-layer buffer strategy[57]. In this approach, an Au or Ag buffer layer was initially prepared through a galvanic displacement process or electrodeposition on commercially available Ni foam (NF), respectively. As shown in Figure 4A, the Pt layer was subsequently electrodeposited onto the buffer substrate by subjecting the potential to cyclic variations between 0 and -0.4 V_{SCE}. The integration of current density over deposition time confirmed the deposition of 578 ng cm^{-2} Pt on Au/NF for each monolayer [Figure 4B]. This result concurred with measurements obtained through quartz crystal microbalance (QCM) measurements (550 ng cm^{-2}) in Figure 4C. Assuming a uniform dispersion of all Pt atoms (578 ng cm^{-2}) across the surface, each Pt atom would occupy an area of 56,014 pm^2 or possess a Pt radius of 134 pm - consistent with the covalent radius of Pt (136 pm). In addition, XPS analysis of three individual areas was performed. The Pt atomic percentages of Pt monolayers on Au/NF (Pt ML/Au/NF) exhibited strikingly similar values across all these three distinct areas. Based on these findings, the authors proposed that the Pt electrodeposition on Au/NF adheres to a comprehensive monolayer mechanism [Figure 4D].

Furthermore, in a subsequent study by the same authors, they presented research involving substrates composed of carbon materials, such as carbon fiber cloth (CF) in Figure 4E-H[58] and carbon fiber paper
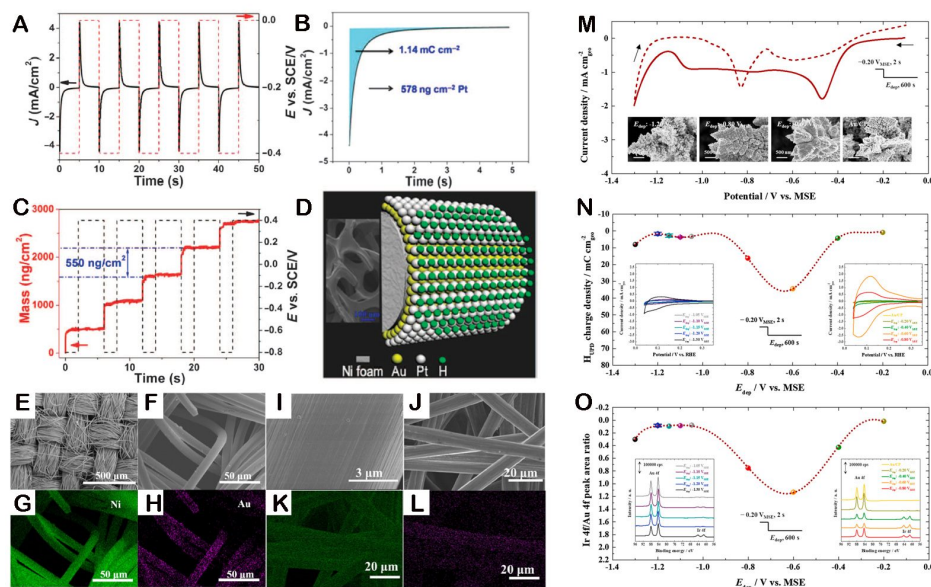
Figure 4. (A) Current density and potential versus time plot for Pt monolayer deposition on 3D Ni foam using the sequential technique. (B) Mass and potential change during Pt monolayer deposition using QCM on Au-coated quartz crystal. (C) Voltammetry curve for Pt deposition on Au NF/Ni foam via pulsed potential waveform in 0.5 M NaCl and 3 mM K_2PtCl_4. (D) Illustration of Pt SED. Inset: SEM image of Ni foam. This figure is quoted with permission from Li *et al.*[57]. FESEM images and EDS mapping on Au/Ni/CF cloth: (E) Low-magnification and (F) Higher-magnification FESEM image. (G) EDS mapping of Ni in image (F). (H) EDS mapping of Au in image (F). This figure is quoted with permission from Pang *et al.*[58]. (I) High-magnification FESEM image of Pt ML on Au/Ni/CFP. (J) Lower-magnification FESEM image of Au/Ni/CFP. (K) EDS mapping of Ni corresponding to image (J). (L) EDS mapping of Au corresponding to image (J). This figure is quoted with permission from Pang *et al.*[59]. (M) CV curve of Au/CP, acquired at 10 mV s^{-1} and 70 °C in N_2-purged 3 mM K_3IrCl_6 and 500 mM Na_2SO_4 (pH = 4.0). Insets showcase FESEM images of Ir on Au/CP deposited at different E_{dep} for 600 s. (*n*) H_{UPD} charge density and (*n*) Ratio of Ir 4f peak area to Au 4f peak area of Ir on Au/CP deposited at various E_{dep} for 600 s. Insets depict CV curves for (M) and XPS profiles for (O). This figure is quoted with permission from Kim *et al.*[51].

(CP) in Figure 4I-L[59], instead of NF. In this context, a thin layer of Ni was initially electrodeposited onto the carbon substrate using the chrono-potentiometry method. Subsequently, a dual buffer layer consisting of Au, prepared by galvanic displacement with Ni, was employed in conjunction with the SED technique to fabricate Pt monolayers.

Porous Au transport layers were prepared by electrochemical methods using gas diffusion layers[51]. Firstly, thin Ni layers were electrodeposited at -1.0 V_{SCE} for 600 s on CP substrates using a Watts Ni bath. Au galvanic displacement was conducted on Ni/CP for 1 h, and then, the remaining Ni was completely removed by electrochemical etching processes. To investigate the Ir SED feasibility, CV was conducted on porous Au/CP at 70 °C in 3 mM K_3IrCl_6 and 500 mM Na_2SO_4 [Figure 4M]. At the initial stage of the negative sweep, the reduction of Ir^{3+} on Au started at approximately -0.25 V_{MSE}, and the reduction current density gradually increased up to -0.47 V_{MSE}, subsequently stabilizing at -0.94 to -0.99 mA cm^{-2} regardless of the potential sweep. At more negative potentials, the reduction current density decreased because of the quenching of Ir reduction[48], which was also observed in the positive sweep at potentials between -1.15 and -1.04 V_{MSE}. The CV feature revealed the quenching of Ir at a highly negative potential, which was well matched with that previously reported for Ir and Pt SED on this Au substrate[44,48].

The quenching of Ir electrodeposition was verified through chronoamperometry measurements lasting 600 s at different E_{dep} values (Inset of Figure 4M). Compared to the Au/CP configuration, samples subjected to Ir electrodeposition at E_{dep} values of -0.60 and -0.80 V_{MSE} exhibited notably smoother surface

morphologies. Field emission scanning electron microscopy (FESEM) analysis unveiled observable Ir deposits on the Au surface. However, despite applying a more negative deposition potential of -1.20 V_{MSE}, the morphology after Ir deposition closely resembled that of Au/CP. Moreover, both electrochemical and spectroscopic measurements affirmed the feasibility of Ir SED. The charge density of H_{UPD} [Figure 4N] and Ir 4f/Au 4f peak ratios [Figure 4O] obtained by XPS for a single Ir pulse at various E_{dep} values mirrored variations akin to those seen in the CV. Notably, the Ir deposited at the quenching potential range (-1.05 to -1.20 V_{MSE}) demonstrated a notably lower H_{UPD} charge density and the XPS peak ratio compared to those within the range where Ir^{3+} reduction was activated (> -0.60 V_{MSE}). Consequently, it has been verified that the SED phenomenon occurs even on porous Au substrates, similar to flat Au substrates[44,48]. Furthermore, it has been confirmed that by adjusting the pulse number, the total amount and loading of Pt[57-59] and Ir[51] can be consistently increased, as demonstrated in prior studies. These characteristics indicate the potential utility of electrodes fabricated through SED for use as gas diffusion electrodes.

SED on substrates of various materials beyond Au

Furthermore, subsequent studies on SED have extended beyond Au substrates to encompass a variety of other materials such as Ni, WC, C, TiN, Ti$_2$AlC, and (Nb-Ti)$_2$AlC [Table 1]. Liu *et al.* investigated the Pt SED on a Ni substrate in a 3 mM K$_2$PtCl$_4$ and 0.5 M NaCl electrolyte with pH 4[46]. The Ni substrate was prepared through the electrodeposition of Ni on an Au-seeded wafer using the Watt bath. Pt electrodeposition on the Au/Ni partitioned electrodes was conducted through immersion at a constant potential of -0.8 V_{SSCE}, which is the potential where Pt SED takes place[44]. To prevent galvanic exchange between $PtCl_4^{2-}$ and the Ni substrate, the Ni/Au partitioned specimens were rapidly immersed and rinsed within 1.5 s after potential control was lost. The authors further compared the Pt 4f region between the Au region and Ni region using XPS after 100 s of Pt deposition [Figure 5A and B]. Compared to Pt on Au, Pt deposited on Ni exhibited a 0.2 eV higher shift in the Pt 4f$_{7/2}$ peak, with the intensity of the Pt peak being almost two times that observed in neighboring Au regions. Subsequently, XPS analysis was carried out to investigate Pt deposition, varying from 1 to 1,000 s, as illustrated in Figure 5C. Pt deposition on Au was completed within a sub-second timeframe, with no additional growth observed between 1 and 1,000 s. Conversely, self-terminating Pt deposition on Ni displayed a notably slower process. Over the initial 100 s of deposition, the Pt 4f intensity exhibited a steady rise, eventually reaching a saturation point nearly twice that of Pt films cultivated on Au.

From XPS analysis, assuming the Pt overlayer on Ni to be laterally uniform, the Pt thickness was calculated, as shown in Figure 5D. The Pt thickness on Ni reaches a saturation level approximately twice that of the Pt films grown on Au. Ion scattering spectroscopy (ISS) also reveals that the surface coverage of Pt slightly exceeds ≈ 50% within 100 s, with additional Pt deposition halting before the coverage surpasses 60%. While keeping the Pt deposition time fixed at 100 s, XPS was conducted as the number of deposition cycles increased. With the number of deposition cycles ranging from 1 to 10, it was observed that the Pt thickness monotonically increased. Up to seven cycles, the binding energy gap of Pt 4f$_{7/2}$ peak between the Au and Ni regions decreased, converging to 71.35 eV, consistent with bulk Pt. Furthermore, as the deposition cycles increased, the surface coverage of Pt on Ni gradually increased, reaching close to 100% by the fifth cycle. Furthermore, in the study of iridium, utilizing a 3 mM K$_3$IrCl$_6$ and 0.5 M Na$_2$SO$_4$ electrolyte at pH 4 and operating at 70 °C, investigation of SED through CV revealed the presence of SED features on the Ni surface, similar to those observed on the Au surface[48].

Kim *et al.* reported Pt SED on CP (CP: carbon paper) without any buffer layer[54]. Figure 5E shows a LSV feature of CP in Pt electrolytes. The reduction of Pt^{2+} ions commenced at -0.30 V_{SCE}, followed by a swift increase in current density upon progressing to more negative potentials. Upon further negative potential sweeps beyond the peak at -0.73 V_{SCE}, the current density exhibited a rapid decrease followed by an increase.
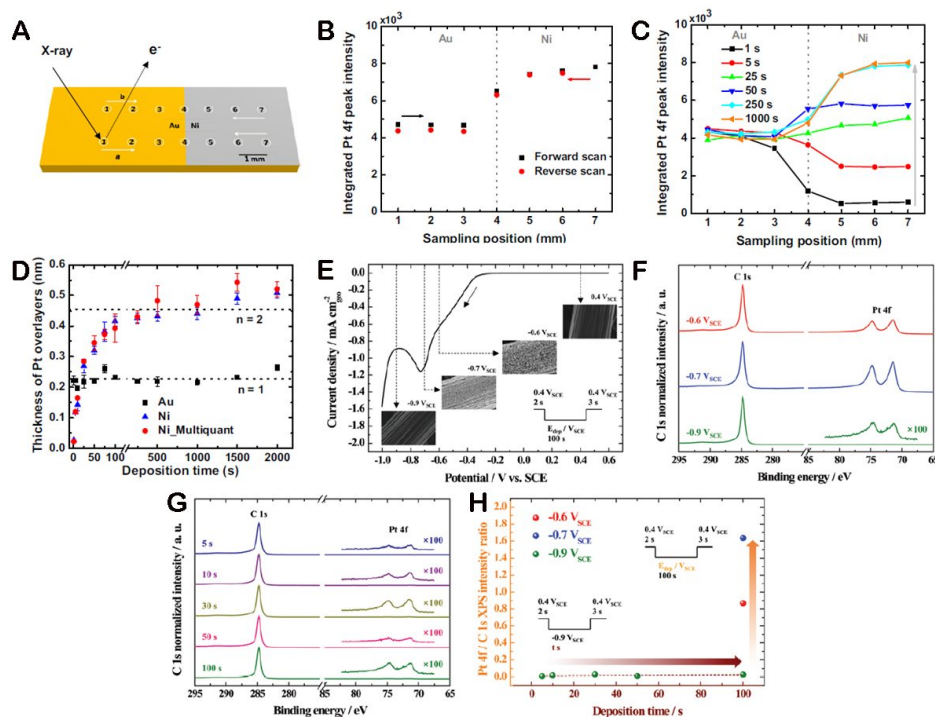
Figure 5. (A) Schematic representation of the sequential acquisition of XPS spectra. (B) Integration of Pt 4f peak intensity at specified sample positions after 100 s of Pt deposition. (C) A representative set of integrated Pt (4f) peak intensities in relation to Pt deposition time. (D) XPS-derived Pt thickness on Ni and Au surfaces. This figure is quoted with permission from Liu *et al.*[46]. (E) LSV curve of CP in a 3 mM K_2PtCl_4 and 0.5 M NaCl electrolyte at a scan rate of 5 mV s^{-1}. Insets exhibit FESEM images after 1 pulse deposition at diverse potentials for 100 s. (F) XPS spectra of C 1s and Pt 4f after 1 pulse deposition at various potentials for 100 s. (G) XPS spectra of C 1s and Pt 4f after 1 pulse deposition at -0.9 V_{SCE} for different durations. (H) Variation of Pt 4f to C 1s peak area ratio, influenced by the deposition potential or time. This figure is quoted with permission from Kim *et al.*[54].

To confirm the self-termination phenomenon on CP, the morphology of the Pt deposits was imaged by FESEM with varying the E_{dep} from 0.40 to -0.90 V_{SCE}. Evidently, Pt deposition occurred on the CP surface at -0.60 V_{SCE}, in contrast to the outcome observed at 0.40 V_{SCE}. At -0.7 V_{SCE}, a noticeable augmentation in Pt coverage was discernible. However, when subjected to a more negative potential (-0.9 V_{SCE}), the Pt deposits were scarcely visible, with the image resembling that of the carbon substrate. Furthermore, this similar trend was obtained in XPS analysis [Figure 5F-H].

The Pt SED was investigated at a TiN substrate in 3 mM K_2PtCl_4 and 0.5 M NaC[56]. By varying the pH of the electrolyte from 1 to 4, the CV was performed from open circuit potentials (OCP) toward negative potentials [Figure 6A]. When the pH of the Pt electrolyte was 1 or 2, the OCP was observed around -0.15 V to -0.2 V_{SCE}. However, as the pH of the Pt electrolyte increased, the OCP gradually shifted towards a positive potential. Upon immersing the TiN substrate in the deposition electrolyte with a pH of 4.0, the observed OCP gradually shifted in a negative direction.

After a duration of 150 s, the OCP reached a stable value of -0.2 V_{SCE} [Figure 6B]. Through XPS analysis [Figure 6C and D], the Ti 2p spectra of the TiN substrate were compared before and after reaching equilibrium. Following the equilibrium phase, the peak ratio of the $Ti(OH)_2^{2+}$ peak showed an increase, indicative of the development of a $Ti(OH)_2^{2+}$ layer. This layer formation effectively inhibited further oxidation[79,80].
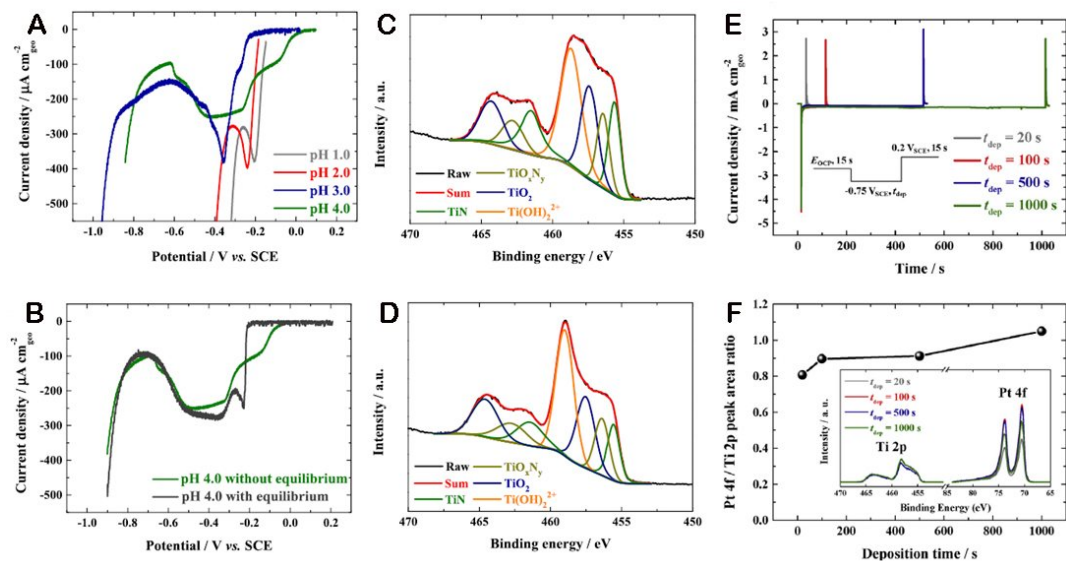
Figure 6. (A) LSV profiles of TiN in a 3 mM K$_2$PtCl$_4$ and 0.5 M NaCl electrolyte. (B) Influence of equilibrium step on LSV curves. XPS spectra of TiN substrates, (C) prior to and (D) post equilibrium step. (E) Current transients with single deposition pulse at 0.75 VSCE as a function of time. Inset: pulse profile. (F) Pt 4f/Ti 2p peak area ratio as a function of deposition time. Inset: corresponding XPS spectra. This figure is quoted with permission from Byun *et al.*[56].

Using a pH 4 solution after the equilibrium step, the authors performed XPS analysis by altering the potential and time of the Pt pulse. After fixing E_{dep} at -0.75 V$_{SCE}$, surface analysis was conducted using XPS while gradually increasing the deposition pulse duration [Figure 6E and F]. Following a single potential pulse lasting 20 s, the Pt 4f/Ti 2p peak area ratio measured approximately 0.81. Increasing the pulse duration to 100, 500, and 1,000 s maintained the peak area ratio within the range of 0.90 to 1.05, indicating minimal alteration in surface composition. This trend corresponds with findings from self-terminated Pt electrodepositions on Au and C substrates[44,47,54]. Atomic force microscopy (AFM) analysis examined the surface morphology of the Pt electrode. A comparison of surface roughness between the as-prepared TiN and Pt1/TiN samples revealed a smoother TiN surface, while distinct bumps emerged after Pt deposition. Height profiles displayed Pt bumps approximately 2.5 nm in height, equivalent to over six atomic layers of platinum. The width of these bumps, approximately 300 nm, signaled noteworthy agglomeration of Pt islands during the pulse. This supports the notion of Pt atom agglomeration due to thermodynamic instability on TiN, undermining their monolayer structure.

Furthermore, in the study of Ir, utilizing a 3 mM K$_3$IrCl$_6$ and 0.5 M Na$_2$SO$_4$ electrolyte at pH 6.2 and operating at 70 °C, the feasibility of SED was investigated by CV on the Ti$_2$AlC surface[65-67]. During the first negative scan of the CV, no peak current was observed due to the presence of a passive oxide film on the surface. However, in the positive scan, a peak current was evident, similar to observations on Au and C substrates. Starting from the second CV, both in the negative and positive scans, the SED feature became apparent. Through the aforementioned studies, it has been demonstrated that the SED phenomenon occurs on various substrates beyond Au, thereby mitigating the drawback of requiring expensive Au substrates for SED. Moreover, the expanded substrate choices allow for the fabrication of various forms of overlayers that induce a synergy effect between PGM overlayers and the substrate.

APPLICATIONS IN WATER ELECTROLYSIS AND FUEL CELL ELECTRODES

Hydrogen oxidation and evolution electrode

Pt and Ir overlayer catalysts produced via SED exhibited excellent activity for hydrogen oxidation (HOR) and hydrogen evolution reactions (HER) under both acidic and alkaline conditions. Despite monolayer-level loading, they demonstrated comparable activity to bulk Pt[46,48,49]. The alkaline HOR/HER catalytic performance of Pt ML/Au and Pt ML/Ni was evaluated using RDE at 1,600 rpm in H_2-saturated 0.1 M NaOH[46]. For Pt ML on both Au and Ni, deposited with a single deposition cycle, the Pt loading is around or below 1 μg cm^{-2}. The Pt ML/Au exhibited a higher HER overpotential than Pt RDE due to electrode texture differences[81]. In contrast, Pt on Ni, forming the Pt50Ni50 surface alloy, displayed significantly lower HER overpotential at -10 mA cm^{-2} with -0.05 V_{RHE} compared with those of Pt RDE (-0.130 V_{RHE}) and Ni (-0.275 V_{RHE}). The enhanced activity suggests synergistic interactions between Ni and Pt sites. The authors proposed that this effect might result from electronic perturbation of the Ni species by Pt or potentially from an active bifunctional mechanism. In this mechanism, Ni sites could facilitate water reduction, leading to the recombination of H adatoms at Pt sites, resulting in the formation of hydrogen molecules[82].

For Pt ML/Au, the initial HOR activity closely matched that of the Pt RDE. However, the HER/HOR activity of Pt ML/Au declined with cycling for both reactions, as illustrated in Figure 7A. In contrast, Pt overlayers on Ni showed HOR inhibition at low overpotentials, peaking around 0.3 V_{RHE}, less than half H_2 transport limit. Later, reaction rates decreased steadily, approaching zero above 0.7 V_{RHE} owing to oxide formation. Subsequent cycles led to progressive HOR decline [Figure 7B]. Nevertheless, the HER activity of $Pt_{50}Ni_{50}$ remained consistent even after 30 cycles. Instead, notable structural and compositional changes are expected to accompany repeated oxide formation and reduction, creating an equally active bifunctional surface phase of Pt species on the Ni-based electrode.

The catalytic activity of the Ir overlayer was assessed for alkaline HER/HOR[48]. As the Ir deposition on the Au RDE increased, both reaction kinetics gradually improved [Figure 7]. After three Ir deposition pulses, the specific current density for HOR/HER exceeded that of the Pt RDE. The specific activity for HOR peaked with five pulses of Ir film growth, while the maximum HER specific activity was observed after three deposition pulses. Moreover, when the Ir overlayer was produced on the Pt surface through SED and its HER/HOR activity was evaluated, it exhibited higher activity not only compared to Pt RDE but also to Ir films on Au [Figure 7C and D]. When comparing specific activities normalized by the H_{UPD} charge density of both Pt and Ir, the Ir film on the Pt surface demonstrated over 1.5 times higher values for both HOR and HER compared to that on Au surfaces [Figure 7E and F].

Additionally, there are cases where the porous 3D bulk substrate was utilized as an electrodeposition substrate, enabling the implementation of SED[57-59]. The initial HER activity test of Pt ML/NF was measured by using CV methods in 0.5 M H_2SO_4. The Pt ML applied on metal/NF shows a much lower HER overpotential of -0.04 V_{RHE} compared with that of Au/NF (-0.13 V_{RHE}) and Ag/NF (-0.14 V_{RHE}). Then, a stability test was conducted by applying the constant current density of -10 mAcm^2 for 8 h. During the stability test, the current density of the Pt ML/Au/NF gradually decreased by approximately 5%, from 0.100 to 0.105 V_{RHE}. Authors suggested that the activity degradation is owing to Ni diffusion to the catalyst surface.

Kim *et al.* reported an extremely low-loading Pt cathode for a proton exchange membrane electrolyzer (PEMWE)[54]. The authors set the single potential pulse for Pt SED on CP as 0.4 V_{SCE} at 2 s, -0.9 V_{SCE} at 10 s, and 0.4 V_{SCE} at 3 s. With an increasing Pt pulse number, Pt#/CP (#: the number of potential pulses) was prepared. Precise control of the Pt loading mass could be achieved in the submicrogram to submilligram range. The half-cell HER activity test was conducted in 0.5 M H_2SO_4 through CV methods, showing a
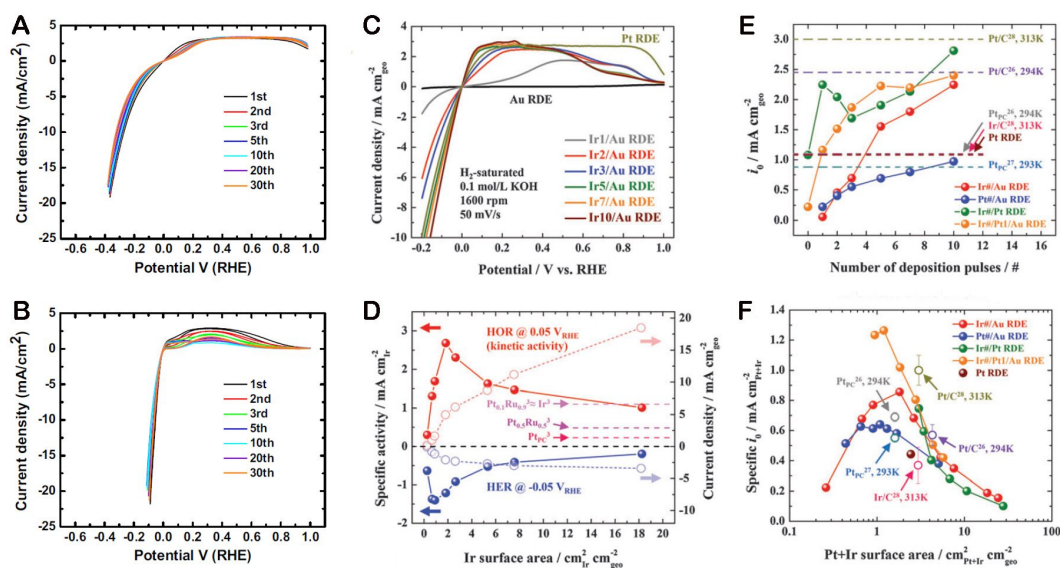
Figure 7. Repeated CV scan of (A) Pt ML/Au and (B) Pt ML/Ni in H_2-saturated 0.1 M NaOH at 50 mV s^{-1} and 1,600 rpm. This figure is quoted with permission from Liu *et al.*[46]. (C) LSV curves of ultrathin Ir films with respect to the number of deposition pulses. (D) Current density for HER (blue) and HOR (in red) at a 50 mV overpotential, normalized to geometric (open) and (H_{UPD}) surface area (solid). The dashed line signifies literature data. (E and F) Exchange current density for diverse Ir and/or Pt overlayers on Au or Pt RDE substrates. This figure is quoted with permission from Ahn *et al.*[48].

gradual increase in the number of potential pulses. Then, the HER activity of the Pt electrode was saturated at 300 pulses with an overpotential of 45 mV at -10 mA cm^{-2} [Figure 8A and B]. Furthermore, a single-cell test for PEMWE was conducted employing the Pt#/CP electrodes as a cathode [Figure 8C and D]. Figure 8C shows the polarization curves of single-cell performances using Pt electrodes, which corresponded well with the HER activity trends obtained from the half-cell test. The maximum current density was obtained with Pt300/CP cathode, which showed 0.60 A cm^{-2} and 2.55 A cm^{-2} at 1.6 V$_{cell}$ and 1.9 V$_{cell}$, respectively. Compared with spray-coated Pt cathodes, the Pt300/CP cathode showed comparable activity with the same Tafel slope of 76 mV dec^{-1}. In addition, the PEMWE results employing Pt300/CP show an order of magnitude higher Pt mass activity at 1.6 V$_{cell}$ and 1.9 V$_{cell}$ than those of previously reported values [Figure 8E and F].

In the subsequent research conducted by the same group, additional refinement of the electrode was accomplished through the utilization of a carbon-coated CP substrate (C/CP) to increase the ECSA[50]. Even after spray-coating the 100-200 nm size of C on the CP substrate, discernible features of Pt SED were observable. In an effort to determine the conditions that maximize the Pt surface area on the C/CP substrate, pulse cycles were incrementally increased, and the double-layer capacitance (C_{dl}) was measured. While generally increasing as the pulse cycles reached up to 30 pulses, the C_{dl} exhibited a slight decrease after 30 pulses during the subsequent 50 pulses. This trend was similarly observed in an acidic HER test conducted via half-cell experiments.

Oxygen evolution electrode

In contrast to HER electrodes, where a wide range of support materials can be selected due to the expansive potential window, studies have emerged employing stable substrates such as Au and Ti_2AlC for OER electrodes[48,51,64,67]. The acidic OER activity of Ir thin films on Au RDE was investigated in oxygen-saturated 0.1 M $HClO_4$ and 0.1 M H_2SO_4 electrolytes. Gradual enhancement of catalytic activity was observed with an increasing number of Ir deposition pulses, ranging from one to ten, in both electrolytes. After three Ir
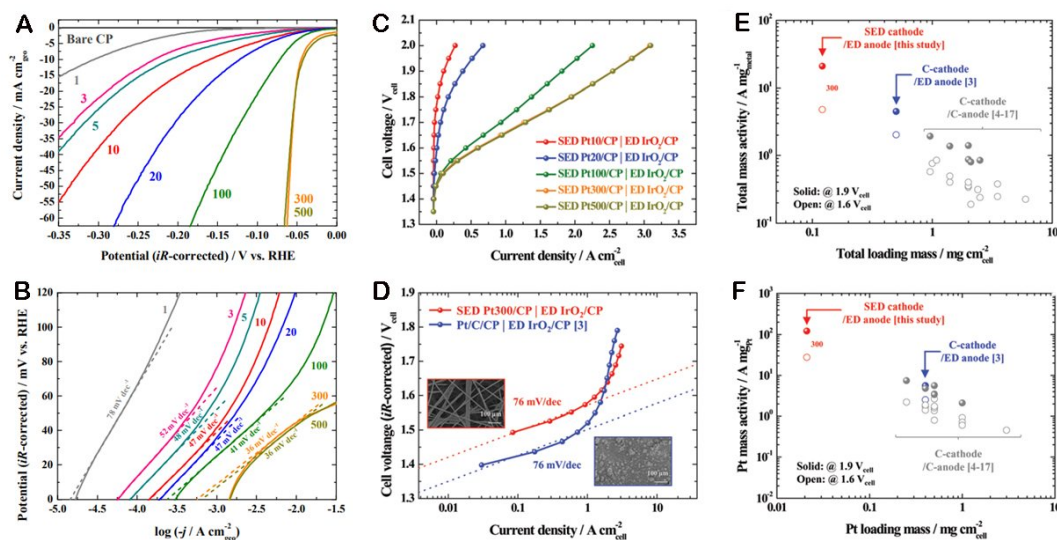
Figure 8. (A) Forward scans of the 1st CV in 0.5 M H_2SO_4 at a scan rate of 50 mV s^{-1}. (B) Corresponding Tafel plots. (C) Polarization curves, illustrating a PEMWE single cell equipped with a SED Pt#/CP cathode and electrodeposited IrO_2 anode. (D) Tafel plots of polarization curves for a PEMWE single cell using a SED Pt300/CP cathode and a Pt/C/CP cathode. Insets are FESEM images of SED Pt300/CP (in red) and Pt/C/CP (in blue). (E) Total mass activity and (F) Pt-specific mass activity. This figure is quoted with permission from Kim *et al.*[54].

deposition pulses, a significantly lower OER overpotential for 5 mA cm^{-2} was achieved compared to that reported for bulk Ir and polycrystalline Ir electrodes. Moreover, the specific activity was evaluated by normalizing the geometric OER activity to the H_{UPD} surface area, revealing an activity surpassing an order of magnitude compared to the reported performance of rutile IrO_2 nanoparticles. Subsequent research has reported the utilization of porous and high-surface-area Au substrates for the development of highly effective OER electrodes with practical applications[51,64].

Wang *et al.* introduced the nanoporous gold (NPG) structure as a substrate[64]. By applying the anodization potential in phosphate buffer solutions (pH 8) containing 1 M KCl, the Au rod was electrochemically anodized. By varying the anodization time between 25 and 300 s, effective control over the roughness factor (R_f) of the NPG surface is achievable. At an anodization time of 300 s, an R_f value of approximately 800 was observed. The acidic OER activity assessment was conducted in a 0.1 M $HClO_4$ solution utilizing CV and chronopotentiometry techniques. In comparison to a flat Au substrate, NPG subjected to 100 s of anodization exhibited a decrease of 190 mV in OER overpotential at 10 mA cm^{-2}. However, upon comparing the Tafel slopes extracted from CV curves, it was evident that the flat Au substrate exhibited the lowest value, while an increase in R_f consistently correlated with an increment in the Tafel slope. This suggested a deceleration in the OER kinetics on the NPG surface despite the lower OER overpotential observed in comparison to the flat Au surface. Different anodization times for various NPG surfaces were evaluated for OER performance by subjecting them to a constant current of 10 mA cm^{-2}. Consistently similar results were obtained with CV experiments. Notably, during the increase in anodization time from 25 to 100 s, a sharp decrease in OER overpotential was observed, with the NPG anodized for 100 s exhibiting an overpotential 96 mV lower than that of flat Au.

Using the NPG anodized for 100 s as a substrate, Pt-modified NPG surfaces (NPG@Pt) were prepared and assessed as OER electrocatalysts through 50 cycles of Pt deposition potential steps between -0.8 and 0.4 V. Initial OER performance results revealed that the NPG (100 s) surface exhibited higher OER activity than

the flat Pt surface. Furthermore, its OER activity was notably enhanced after Pt modification. The NPG@Pt surface exhibited an OER overpotential at 10 mA cm^{-2} more than 300 mV lower than that of both the original NPG and flat Pt surfaces. However, it demonstrated higher Tafel slopes compared to the original NPG and flat Pt surfaces, indicative of slower OER kinetics. The authors explained that the lower OER overpotential of the NPG@Pt surface, even with its slower OER kinetics, can be attributed to its porous structure.

Kim *et al.* reported a dendritic Au-supported Ir gas diffusion electrode as an anode of PEMWE[51]. The potential step at -1.20 V$_{MSE}$ was employed as a SED potential for Ir deposition, while subsequent treatment at the -0.30 V$_{MSE}$ re-activated the Ir surface via the oxidation of the adsorbed H. Repetition of the potential transient between -1.20 V$_{MSE}$ (10 s) and -0.30 V$_{MSE}$ (2 s) facilitated the gradual increase in Ir loading on Au/CP [Figure 9A and B].

Then, the nomenclature for the samples was determined as #Ir/Au/CP (#: the number of deposition pulses). As the number of deposition pulses was increased, a gradual increase of the Ir content was confirmed by the H$_{UPD}$ feature. For Ir1/Au/CP, the H$_{UPD}$ charge density equaled 1.15 mC cm^{-2}, and the corresponding roughness factor (R$_f$) was obtained as 5.32 from the H$_{UPD}$ charge density of a flat Ir monolayer (217 μC cm^{-2}). Furthermore, the Ir coverages were calculated from the charge density of Au oxide reduction for Ir#/Au/CP, based on that for bare Au/CP. For Ir1/Au/CP, the Ir coverage is about 8.1%. It rapidly increased after five deposition pulses and then slowly increased to 73.5% for Ir50/Au/CP.

In order to examine the electronic structure of Ir#/Au/CP, the Ir 4f spectra were deconvoluted to the two doublets: Ir 4f$_{5/2}$ and Ir 4f$_{7/2}$. It was revealed that metallic Ir^0 ratios gradually increased with the number of deposition pulses, while the sum of oxidized Ir valency (Ir^{3+} and Ir^{4+}) content was continuously decreased. This result might be attributed to the electron transfer from Ir to Au, becoming insignificant at higher Ir surface composition. As shown in Figure 9C, the binding energy of the Ir 4f$_{7/2}$ peak and the ratio of Ir^{3+} + Ir^{4+} + Ir$^{>4+}$ continuously decreased with an increase in Ir coverage, indicating that more electrophilic Ir islands were formed at lower Ir coverage. The authors suggested that the Ir electronic structure was significantly changed by the surface density of the Ir/Au interface and the electron density gradient of Ir islands.

The initial OER activity of Ir-deposited Au layers was investigated in a 0.5 M H$_2$SO$_4$ electrolyte using LSV methods at a scan rate of 5 mV s^{-1}. [Figure 9D and E]. The Au/CP showed negligible OER activity, while the OER performance gradually increased with the number of Ir deposition pulses. The geometric OER activity was maximized with the Ir30/Au/CP having the lowest overpotential of 318.7 mV at a current density of 10 mA cm^{-2}, and it showed superior mass activity compared to the state-of-the-art Ir-based catalysts. The authors attributed this enhancement to the extremely low Ir loading (8.46 μg cm$_{geo}^{-2}$) and the modified electronic structure.

In addition, the authors compared the OER performance of the optimized samples by subjecting them to either electrochemical or thermochemical oxidation methods. As demonstrated in Figure 9F, the electrochemically oxidized IrO$_x$ electrode (EC-IrO$_x$/Au/CP) exhibited the highest OER activity, followed by the metallic Ir30/Au/CP electrode and thermochemically oxidized Ir electrode (TC-IrO$_x$/Au/CP). They compared the specific OER activity by normalizing the geometric OER activity C$_{dl}$ of each electrode. All Au-supported Ir exhibited higher specific OER activity than that of pure Ir, while the EC-IrO$_x$/Au/CP also exhibited the highest specific OER activity. Figure 9G showed the specific OER activity as a function of the Ir^{3+}/(Ir^{3+} + Ir^{4+}) ratio in Ir-based electrodes, demonstrating the linear relationship. However, when
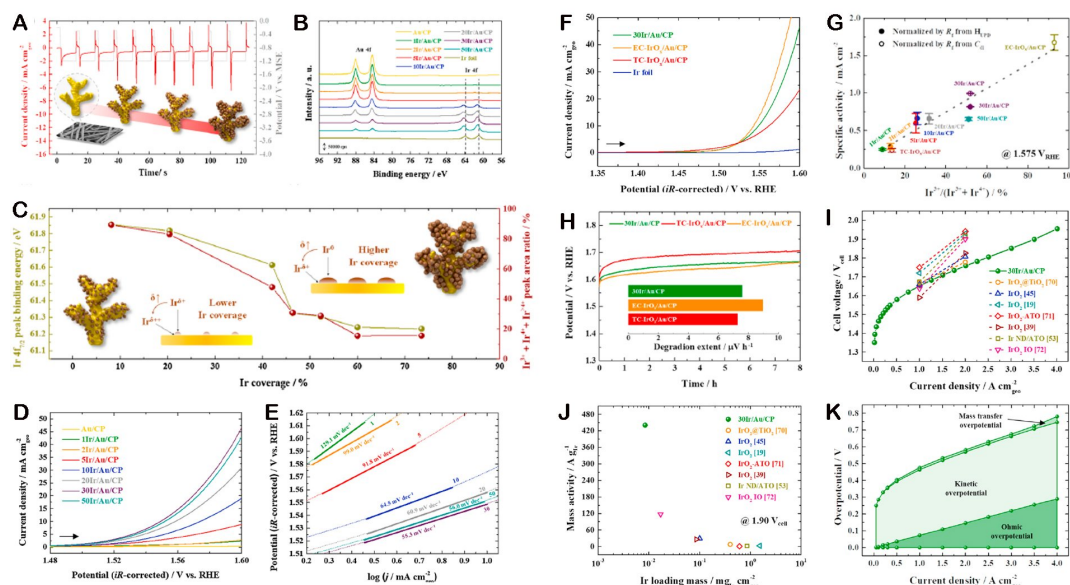
Figure 9. (A) Time-dependent current behavior during Ir deposition on Au/CP using repetitive potential pulses in a N_2-purged solution of 3 mM K_3IrCl_6 and 500 mM Na_2SO_4 (pH = 4.0) at 70 °C. (B) Au 4f and Ir 4f spectra from Au/CP, Ir/Au/CP, and commercial Ir foil samples. (C) Ir $4f_{7/2}$ peak binding energy and [$Ir^{3+} + Ir^{4+} + Ir^{>4+}$] area ratio of #Ir/Au/CP depending on Ir coverage. (D) LSV curves for OER activity of each electrode. (E) Tafel plots corresponding to (D). (F) CV curves of Ir-based electrodes recorded at 10 mV s^{-1} in N_2-purged 0.5 M H_2SO_4. (G) Specific activity as a function of the $Ir^{3+}/(Ir^{3+} + Ir^{4+})$ ratio. (H) Results of OER stability testing at 10 mA cm^{-2} for 8 h. (I) Polarization curve for PEMWE single cells with 30Ir/Au/CP anodes and cell voltages from literature. (J) Mass activity comparison at 1.90 V_{cell} depending on Ir mass loading for different Ir-based catalysts. (K) Overpotential subdivisions of (I). This figure is quoted with permission from Kim *et al.*[51].

chronopotentiometry was applied at 10 mA/cm² for 8 h [Figure 9H], the EC-IrO$_x$/Au/CP electrode, which initially displayed the highest OER activity, showed a higher degradation ratio. This result aligns with the previously reported trade-off correlation between OER activity and stability[83-85]. Noteworthy is the fact that the metallic Ir30/Au/CP electrode exhibited an extremely high stability comparable to that of TC-IrO$_x$/Au/CP. The authors suggested that this unexpected stability was attributed to the promotional effect of the electronic structure change of Au-supported Ir.

Finally, the metallic 30Ir/Au/CP was employed as an anode of PEMWE in Figure 9I. In comparison with previously reported results, the PEMWE employing the 30Ir/Au/CP anode demonstrated a modest level of activity at a current density of 1.0 A cm^{-2}. However, it exhibited the highest activity at a current density of 2.0 A cm^{-2}. Furthermore, when comparing the mass activity based on Ir loading at 1.9 V_{cell}, it also exhibited the highest activity. The authors attributed these findings to the analysis of overpotential, revealing that the extremely low mass transfer overpotential was the driving factor [Figure 9J and K]. They explained this phenomenon as stemming from the benefits of the porous Au layer structure.

Formic acid oxidation electrode

Pt-Au alloy catalysts have garnered significant attention due to their remarkable selectivity for the direct pathway of formic acid oxidation reactions (FAOR). This heightened performance can be attributed to the ensemble effect, wherein the isolation of the Pt site inhibits the adsorption of *CO intermediates and expedites the direct pathway[86-88]. Recently, the incorporation of Pt onto Au surfaces, extending beyond the traditional Pt-Au alloy configuration, significantly enhances catalyst utilization by virtue of an augmented Pt area/volume ratio. Insights from *in situ* spectroscopic analyses of reaction intermediates have unveiled the affirmative influence of ensemble and strain effects[61], findings corroborated by density functional theory (DFT) calculations[89].

Ahn *et al.* reported the ultrathin Pt films on the (111) texture of Au for FAOR catalysts[47]. As the Pt pulsing between 0.4 V and -0.8 V_{SSCE} increased, the FAOR activity of bulk Pt, the thin Pt film on Au, and Au substrates was measured using CV methods in 0.5 M HCOOH and 0.5 M H_2SO_4 with a scan rate of 10 mV s^{-1}. Compared with bulk Pt, Pt films subjected to 1-3 pulses exhibited higher activity. Notably, during five CV cycles for FAOR, the thinnest Pt film created with a single pulse demonstrated a current density over ten times higher. Furthermore, the scaled current density normalized by the charge density of the H_{UPD} area showed values exceeding two orders of magnitude compared to bulk Pt. On the other hand, Pt films with a thickness of more than three monolayers (5-7 pulses) exhibited similar low activity to bulk Pt.

The authors also observed changes in FAOR activity based on upper potentials. Restricting the upper potential to 0.75 V_{RHE} and conducting ten cycles of CV revealed a trend where all catalysts experienced a significant decrease in current density after the first scan. Additionally, when the upper potential was set to 1.3 V_{RHE}, within the range where Pt dissolution can occur, an additional ten CV cycles were performed, revealing changes in the peak shape for FAOR. This wider voltammetric window highlighted two distinct regions of formic acid oxidation behavior: a direct dehydrogenation mechanism operating at low potentials and an indirect dehydration reaction dominating at higher potentials. Overall, when the upper potential was set at 1.3 V_{RHE}, an increase in current density with cycling was observed. In the case of the one Pt pulsed film, an increase in currents, along with a negative shift in the potential of the FAOR peak, was observed. However, at 0.9 V_{RHE}, the peak involving the oxidative removal of the poisoning reaction intermediate, i.e., CO, from the surface decreased. Conversely, for Pt films subjected to five and seven pulses, a narrow peak emerged near 0.9 V_{RHE}.

To explore the enhanced FAOR activity more extensively, the authors conducted a CV test with 1,200 cycles [Figure 10A and B]. During the initial 70 cycles, the current density at 0.9 V rapidly decreased, indicating the disappearance of the indirect FAOR pathway. Meanwhile, the peak current density continued to increase during the initial 70 cycles, while the peak potential decreased and remained stable from 0.63 to 0.48 V_{RHE}. However, after 200 cycles, the peak current density gradually decreased, and the peak potential shifted positively again.

In order to understand the cause of this activity change, XPS analysis was conducted on the post-FAOR samples. Compared to the as-prepared sample, after the initial increased activity of 70 cycles, the Pt 4f peak shifted from 70.9 to 70.5 eV, corresponding to Pt alloyed into miscut Au (111) surfaces for a nominal Pt fractional coverage that spans the range from 0.4 to 0.29. On the other hand, in the O 1s and C 1s regions, there was no change during the first 70 cycles, but a new peak emerged starting from 200 cycles when the activity began to decrease [Figure 10C]. The C/O area ratio, adjusted for sensitivity factors, exceeded 3. In the cycling test of FAOR conducted by varying the scan rate, the current decrease followed a $t^{-1/2}$ trend, indicating a diffusion-limited process. This observation led to the conclusion that the deactivation of FAOR during cycling was due to the accumulation of poisoning impurities resulting from the reduction of formic acid at the counter electrode. The authors further confirmed that when conducting a CV test on a one-pulsed Pt film using only H_2SO_4 without HCOOH, the absence of the C 1s spectra was also noted.

In their subsequent study, the authors conducted research by electrodepositing atomic Pt clusters on dendritic Au/CP in a similar manner, applying them as anodes for direct formic acid fuel cells (DFAFCs). Following a procedure similar to the Au thin film, they varied the number of Pt pulses during deposition and tested FAOR activity. Similar to observations in the thin Au film, a lower fractional coverage of Pt on
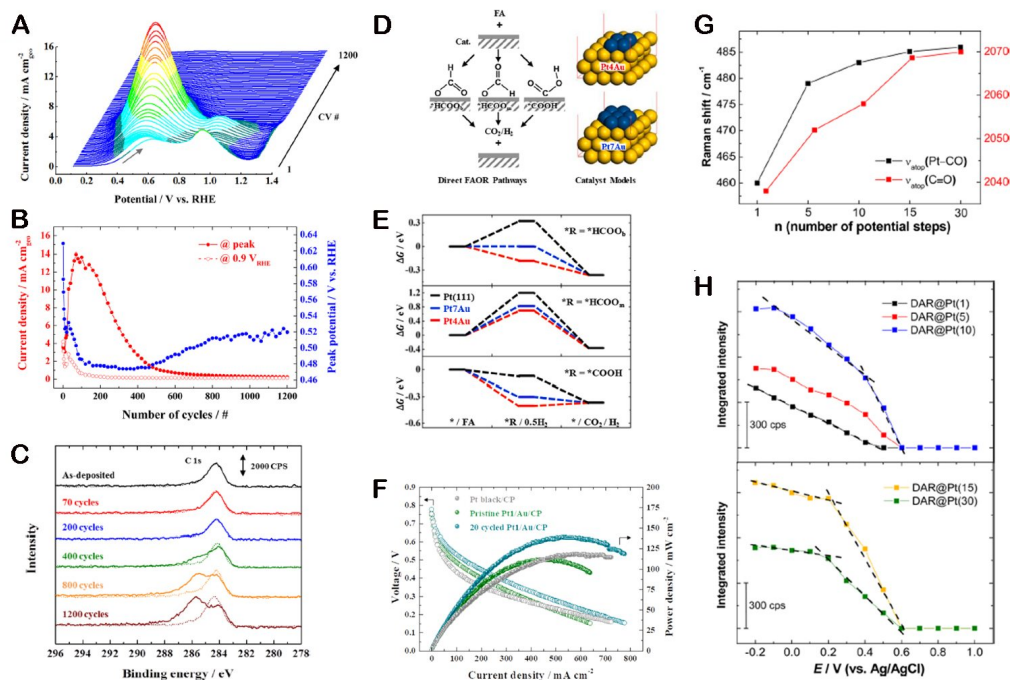
Figure 10. (A) Progression of formic acid oxidation on Pt during voltammetric cycling at a 20 mV s^{-1} scan rate (only forward scan shown). (B) Summarized peak potential, current density at the peak potential, and current density at 0.9 V$_{RHE}$ with respect to the cycle number. (C) C 1s spectra for the Pt film produced with a single deposition pulse, both before and after formic acid oxidation. This figure is quoted with permission from Ahn *et al.*[47]. (D) Schematic illustration for direct FAOR pathways through *HCOOb, *HCOOm, and *COOH intermediates and Pt@Au catalyst models. (E) Free energy diagrams of every direct FAOR pathway. (F) DFAFC performance with Pt1/Au/CP-based anodes. This figure is quoted with permission from Kim *et al.*[53]. (G) Raman shift of Pt-CO and C≡O corresponding to CO adsorption on DAR@Pt(*n*) surfaces. (H) Variations in the integrated SERS intensity for the Pt-CO (atop) bands in relation to the potential on DAR@Pt(*n*) substrates. This figure is quoted with permission from Jeong *et al.*[61].

the Au surface led to a higher current density through the direct pathway. As FAOR proceeded through CV, they observed a gradual increase in current density through the direct pathway due to a decrease in Pt coverage caused by Pt dissolution. Particularly, when conducting CVs with a fresh electrolyte after each cycle, a significantly higher current density at 0.5 V$_{RHE}$ was observed corresponding to the direct pathway compared with using a single electrolyte. This discrepancy arises from the prevention of re-deposition of dissolved Pt in the solution during CV tests when fresh electrolyte is employed, thus maintaining the atomic cluster form of Pt deposit. A Pt1/Au/CP sample treated with a single pulse demonstrated a current density exceeding 100 mA cm^{-2}.

In addition, the authors aimed to explore the impact of Pt catalyst structures after 20 CV cycles by examining the CO bonding geometry, which is influenced by the size of metallic Pt. CO molecules were introduced onto Pt1/Au/CP samples, and an *in situ* DRIFTS technique was employed. In the case of pristine Pt catalysts, the CO binding with a Pt peak was not observed due to oxygen coordination of Pt; however, this was confirmed after pre-reduction with H$_2$ before analysis. For both Pt1/Au/CP samples before and after 20 CV cycles, strong peaks around 2,070 cm^{-1} indicated CO molecules binding linearly to the metallic Pt, while peaks corresponding to bridged CO were scarcely visible. From these findings, the authors concluded that Pt exists in the form of small clusters behind the Au/CP surface and maintains a stable structure of aggregation at low-coordinated Pt sites during 20 cycles of FAOR.

The authors also conducted an analysis of intermediates for the FAOR pathway of Pt clusters on dendritic Au/CP using DFT calculations based on simplified models for catalysts [Figure 10D and E]. These models were constructed by depositing Pt clusters (containing four or seven Pt atoms) onto the Au(111) surface model, denoted as Pt4@Au and Pt7@Au, mirroring the experimental fabrication process of Pt1/Au/CP. The number of Pt atoms corresponds to surface coverages of 0.25 and 0.44, similar to the calculated Pt coverage of five-cycled Pt1/Au/CP (0.21) and pristine Pt1/Au/CP (0.45). It was confirmed that the Pt@Au models, featuring Pt clusters on Au(111) surfaces, reveal that all reaction intermediates are significantly stabilized compared to Pt(111) surfaces (0.00/-0.18 eV for *HCOOb, 0.82/0.69 eV for *HCOOm, and -0.30 / -0.40 for *COOH in Pt7@Au / Pt4@Au, respectively), thus explaining the facile direct FAOR in Pt1/Au/CP. Particularly in the Pt4@Au model, the *HCOOb direct pathway could dominate with a reaction energy profile that lacks a thermodynamic barrier, owing to the enhanced interaction between Pt islands and oxygen-containing functional groups.

To exemplify the suitability of Pt/Au/CP in DFAFCs, Pt1/Au/CP was utilized as an anode in membrane electrode assembly (MEA). 2.0 M HCOOH solution and dry oxygen gas were supplied to the anode and cathode, respectively. The DFAFC using 20-cycled Pt1/Au/CP exhibited a current density of 272 mA cm^{-2} at 0.4 V$_{cell}$, which is 1.37 times higher than that of using the pristine Pt1/Au/CP anode [Figure 10F]. Despite its ultra-low platinum loading mass (5.0 ± 0.2 μg$_{Pt}$ cm^{-2}), the 20-cycled Pt1/Au/CP anode exhibited two-order higher Pt mass activity at 0.4 V$_{cell}$, along with a two-order higher mass power density, outperforming most catalysts reported in recent literature. The authors emphasize the exceptional catalyst utilization of intrinsically active sites.

In situ electrochemical surface-enhanced Raman scattering (SERS) was employed to investigate the FAOR on a Pt layer on DAR[61]. The Pt SED was performed on DAR by repetitive potential pulse of -0.75 V for 10 s followed by 0.4 V for 30 s. With an increase in the number of potential pulses, the Pt coverage monotonically increased, but there are no morphological changes in catalysis. Conversely, XPS analysis showed a lower Pt 4f peak shift for DAR@Pt(1) compared to DAR@Pt(n ≥ 5), indicating modified electrochemical structures. SERS properties of DAR@Pt(n) were probed with CO, revealing higher vibrational frequency shifts for Pt-CO and C≡O bands as the number of Pt deposition pulses increased [Figure 10G]. These suggested deposited Pt on DAR surface transitions from island-type to overlayer structures, fully covering Au surfaces after 15 pulses. When conducting FAOR tests on DAR@Pt(n) catalysts using CV in 0.1 M HCOOH and 0.1 M H$_2$SO$_4$ solutions, clear peaks corresponding to the direct and indirect pathways were distinctly observed in DAR@Pt(n ≥ 5) samples. For the DAR@Pt(1) sample, akin to observations in Pt-modified Au catalyst research, only the peak attributed to the direct pathway was evident at 0.3 V$_{Ag/AgCl}$. The authors also conducted *in situ* SERS measurements during FA electrooxidation on DAR@Pt(n) surfaces, displaying potential-dependent SERS spectra [Figure 10H].

Pt-CO bands were observed for all DAR@Pt(n) surfaces, indicating that the dehydration of FA occurs on all of these surfaces. Pt-CO (atop) bands were observed even on the DAR@Pt(1) surfaces, which indicates that the indirect pathway of FA electrooxidation occurs on these surfaces. However, the amount of CO varied with Pt coverage, and as Pt coverage decreased, the intensity for the Pt-CO band decreased as the electrode potential shifted towards positive regions, as confirmed through potential-dependent SERS. In the case of DAR@Pt(1), the SERS intensity monotonically decreased from -0.2 V$_{Ag/AgCl}$ and vanished at 0.4 V$_{Ag/AgCl}$. For structures closer to a Pt overlayer, such as DAR@Pt(15) and DAR@Pt(30), the SERS intensity remained steady up to 0.2 V$_{Ag/AgCl}$ and then drastically decreased. From these findings, the authors postulated that CO formation via formic acid dehydration is suppressed on DAR@Pt(1) surfaces, and the interaction strength between CO and Pt weakens rapidly during positive potential excursions.

Methanol oxidation electrode

The geometric MOR activity of Pt on the (111) textured Au substrate was evaluated in a solution containing 0.5 M CH_3OH and 0.1 M $HClO_4$. The CV was conducted to assess the MOR activity as a function of Pt thickness by gradually growing Pt layers [Figure 11A]. The Au substrate showed negligible catalytic activity for MOR, while the onset of MOR was consistently observed around +0.60 V_{RHE} for all investigated Pt films. In contrast, the Pt sub-monolayer film prepared using a single deposition pulse demonstrated the highest peak current density. When the geometric current density for MOR was normalized by the charge density in the H_{UPD} region and compared, the Pt film prepared with a single deposition pulse also exhibited the highest activity [Figure 11B].

Compared with bulk Pt, the Pt film demonstrated a peak current density four times higher. This higher activity of the thinnest Pt films can be attributed to the close proximity of exposed Au substrate sites and the Pt overlayer. On the other hand, Pt films with thicknesses of two monolayers or more, produced through three or more deposition pulses, exhibited MOR activity that was nearly comparable to that of bulk Pt. These findings imply that the MOR enhancement is attributed to the inherent mesoscopic structure formed by the step-edge boundary between the high density of Pt islands and the Au substrate.

In the assessment of MOR activity of Pt films over ten cycles [Figure 11C], the Pt film grown using a single deposition pulse displayed a progressive deterioration in methanol oxidation kinetics after the third scan of CV. Conversely, as the thickness of the Pt film increased, similar to bulk Pt, there was a notably less pronounced attenuation of MOR activity with CV cycling. The deactivation of the Pt sub-monolayer structure was clearly more severe than observed for the thicker Pt overlayers [Figure 11D]. This is attributed to the vulnerability of surface rearrangements between the Pt islands and exposed Au substrate at the electrode/electrolyte interface.

The Pt catalyst also demonstrated an expedited direct pathway for MOR on a TiN substrate by mitigating CO adsorption through the hydroxyl group[81,90,91]. Moreover, its high electrical conductivity and oxidation resistance render it a potentially fitting supporting material. Byun *et al.* reported the Pt overlayer on a TiN substrate for MOR catalysts[56]. When using Pt pulse deposition conditions of -0.75 V for 20 s and 0.2 V for 15 s, repeated pulsing resulted in a monotonic increase in the Pt amount, as observed through XPS and ICP-MS analysis, akin to the trends observed on Au and C substrates. Single-pulsed Pt samples (Pt1/TiN) displayed a Pt loading of 0.93 μg cm^{-2}, while the height of Pt bumps observed via AFM increased from 2.5 nm for Pt1/TiN to 10.0 nm for Pt15/TiN.

The CV tests for MOR activity were conducted using CH_3OH and 0.5 M $HClO_4$ electrolytes. The Pt1/TiN sample showed minimal catalytic activity in MOR. In contrast, when the number of deposition pulses exceeded 7, a noticeable geometric current density for MOR was observed. Furthermore, as the deposition pulse number increased, the geometric MOR activity of Pt#/TiN gradually improved [Figure 11E]. The authors pointed out that the peak ratio of forward and backward scans for the TiN-supported Pt catalysts was significantly higher than that of bulk Pt, mainly due to increased resistance to CO poisoning. Furthermore, mass MOR activity of the Pt#TiN was compared as a function of the number of deposition pulses, showing a volcano-like relationship with the number of deposition pulses [Figure 11F]. As the number of Pt deposition pulses increased up to 20, the mass activity gradually rose, reaching 5.73 mA mg^{-1}, and then decreased significantly for Pt40/TiN. The authors suggested that this is due to a complete Pt coverage on the bottom surface of the Pt40/TiN catalyst. Notably, the Pt(100) plane, known for its superior intrinsic activity compared to the Pt(111) plane[91], was preferentially deposited on the TiN substrate[92]. In contrast, Pt20/TiN exhibited a higher density of Pt/TiN boundaries than Pt40/TiN, contributing to the enhanced catalytic activity of Pt20/TiN.
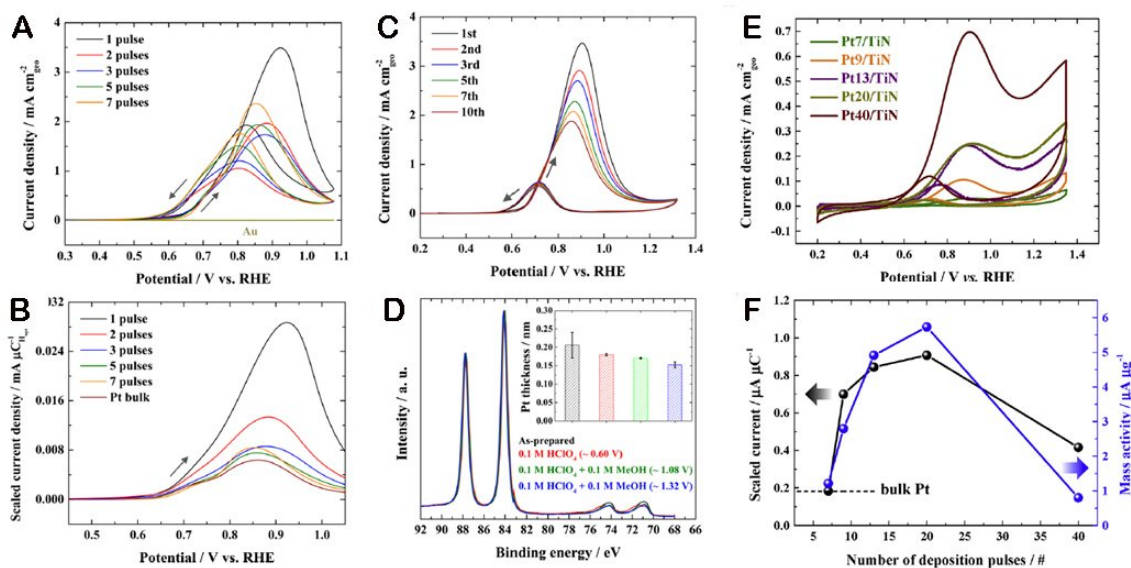
Figure 11. (A) CV curves of Pt ultrathin films, bulk Pt, and Au in Ar-purged 0.5 M CH_3OH and 0.1 M $HClO_4$ solution at a scan rate of 10 mV s^{-1}. (B) The same voltammetric cycle scaled by H_{UPD} charge. (C) MOR CV of a Pt film grown using a single deposition pulse in Ar-purged 0.5 M CH_3OH and 0.1 M $HClO_4$ solution, with a scan rate of 10 mV s^{-1} for ten cycles. (D) Pt 4f and Au 4f spectra for the Pt film formed via a single deposition pulse, both before and after ten CV cycles, using the specified upper potential limit. This figure is quoted with permission from Ahn *et al.*[47]. (E) MOR CV curves of Pt#/TiN samples in a N_2-purged 0.5 M CH_3OH + 0.5 M $HClO_4$ electrolyte, scanned at 10 mV s^{-1}. (F) Scaled current and mass activity of Pt#/TiN at 0.8 V_{RHE} against the number of deposition pulses. This figure is quoted with permission from Byun *et al.*[56].

CONCLUSION AND OUTLOOK

Over the decades, PGM catalysts have garnered considerable attention for their role in water electrolysis and fuel cells. However, their elevated cost and constrained availability present barriers to the advancement of energy conversion systems. To address this challenge, a diverse array of strategies has been explored within the realm of PGM catalysts. Notably, catalysts exhibiting an overlayer structure emerge as highly promising candidates, attributed to their exceptional catalyst utilization efficiency, bimetallic effects, and strain-induced enhancements. SED enables precise atomic layer electrodeposition within an aqueous electrolyte environment. This technique facilitates the meticulous control of metal loading quantities and surface coverage, all achievable at low temperatures and devoid of vacuum conditions.

Catalytic materials endowed with tailored properties, encompassing coverage and thickness modulation through SED, showcase distinct electrochemical reactivity compared to bulk catalysts. Of particular significance is their remarkable electrocatalytic activity, especially evident in terms of mass and specific activity. This comprehensive review encapsulates the essence of the SED phenomenon, elucidates the methodologies for fabricating PGM catalysts via SED, and outlines their applications in water electrolysis and fuel cells. Nonetheless, it is imperative to note that further investigations are requisite in the subsequent domains.

Advancing mechanistic understanding into SED

Since the initial discovery by Moffat group[44] that the SED phenomenon occurs due to H passivation of Pt and Ir on Au films, there has been a focus on benchmarking the fabrication methods of pioneering groups and producing catalysts on different types of substrates. Following material synthesis, research has been confined to ex-situ methods for analyzing material properties and applying them as catalysts. On the other

hand, Lapp *et al.* utilized DFT calculations to reveal the random growth of Pt on Au nanoparticles during SED[70]. Hence, there is an increasing demand for studies that thoroughly elucidate the SED phenomenon through the utilization of computational chemistry and *in situ* techniques.

Emergent need for alloy and multi-element catalyst development

Despite the reported cases of alloy catalysts produced in the form of films using the SED method for Fe group metals, no instances have been documented for PGM catalysts. Given the remarkable catalytic activity of alloyed metals in various fields, the utilization of SED for exceptional alloy layers or layer-by-layer catalysts holds great promise. Moving beyond investigations limited to singular Pt and Ir catalysts, there is a pressing need to explore multi-element catalyst development involving Pt, Ir, and Fe group metals.

Diversifying substrate variability in SED: beyond thin films

Despite the highly convenient and impactful catalyst production capabilities of the SED method, a majority of studies have primarily focused on fabricating catalysts at the level of a few monolayers on film-like substrates. While a few papers have explored nanoparticle and dendrite substrates, these have been limited to Au substrates. There exists a pressing need for the reporting of research employing SED on a wider range of substrate forms to enhance its versatility.

Advancing SED-generated catalysts for practical applications and commercial viability

Given the prevalent focus on catalyst development in film forms, instances of SED-applied single-cell operation in practical devices remain scarce. While some papers have reported single-cell tests, a comprehensive evaluation of long-term performance at an industrially scalable level is still lacking. Nonetheless, despite this challenge, long-term activity tests in most catalysis research predominantly focus on activity maintenance and decline, with limited reporting on catalyst reconstruction during the active phase. The paucity of such analyses underscores the need for relevant investigations to evaluate the commercial viability of SED-based catalyst fabrication methods.

DECLARATIONS

Authors' contributions

Conceptualization, investigation, writing - original draft: Kim H
Conceptualization, methodology, writing - revise and optimize the manuscript: Kim H, Hong S
Investigation, methodology: Hong S, Bang J, Jun Y, Choe S
Review & editing, supervision: Ahn SH, Kim SY

Availability of data and materials

Not applicable.

Financial support and sponsorship

Conflicts of interest

All authors declared that there are no conflicts of interest.

Ethical approval and consent to participate

Not applicable.

Consent for publication
Not applicable.

Copyright
© The Author(s) 2024.

REFERENCES

1. Ausfelder F, Bazzanella A. Hydrogen in the chemical industry. In: Detlef Stolten, Bernd Emonts, editors. Hydrogen science and engineering : materials, processes, systems and technology. Weinheim: Wiley-VCH; 2016. pp. 19-39.
2. Chaubey R, Sahu S, James OO, Maity S. A review on development of industrial processes and emerging techniques for production of hydrogen from renewable and sustainable sources. *Renew Sustain Energy Rev* 2013;23:443-62. DOI
3. Hasanuzzaman M, Zubir US, Ilham NI, Seng Che H. Global electricity demand, generation, grid system, and renewable energy polices: a review. *WIREs Energy Environ* 2017;6:e222. DOI
4. Liu Z, Ciais P, Deng Z, et al. Carbon monitor, a near-real-time daily dataset of global CO_2 emission from fossil fuel and cement production. *Sci Data* 2020;7:392. DOI PubMed PMC
5. Aghahosseini A, Solomon A, Breyer C, et al. Energy system transition pathways to meet the global electricity demand for ambitious climate targets and cost competitiveness. *Appl Energy* 2023;331:120401. DOI
6. Lippkau F, Franzmann D, Addanki T, et al. Global hydrogen and synfuel exchanges in an emission-free energy system. *Energies* 2023;16:3277. DOI
7. Chi J, Yu H. Water electrolysis based on renewable energy for hydrogen production. *Chinese J Catal* 2018;39:390-4. DOI
8. Younas M, Shafique S, Hafeez A, Javed F, Rehman F. An overview of hydrogen production: current status, potential, and challenges. *Fuel* 2022;316:123317. DOI
9. Anwar S, Khan F, Zhang Y, Djire A. Recent development in electrocatalysts for hydrogen production through water electrolysis. *Int J Hydrog Energy* 2021;46:32284-317. DOI
10. Kumar S, Lim H. An overview of water electrolysis technologies for green hydrogen production. *Energy Rep* 2022;8:13793-813. DOI
11. Wu T, Qiu Z, Hsieh C. Obtaining Ni P electrocatalyst in minutes via electroless plating on carbon nanotubes decorated substrate for alkaline urea electrolysis. *Appl Surf Sci* 2024;645:158831. DOI
12. Kovač A, Paranos M, Marciuš D. Hydrogen in energy transition: a review. *Int J Hydrogen Energy* 2021;46:10016-35. DOI
13. Moradi R, Groth KM. Hydrogen storage and delivery: review of the state of the art technologies and risk and reliability analysis. *Int J Hydrog Energy* 2019;44:12254-69. DOI
14. Tang D, Tan G, Li G, et al. State-of-the-art hydrogen generation techniques and storage methods: a critical review. *J Energy Stor* 2023;64:107196. DOI
15. Ong B, Kamarudin S, Basri S. Direct liquid fuel cells: a review. *Int J Hydrog Energy* 2017;42:10142-57. DOI
16. Alias M, Kamarudin S, Zainoodin A, Masdar M. Active direct methanol fuel cell: an overview. *Int J Hydrog Energy* 2020;45:19620-41. DOI
17. Ud Din MA, Idrees M, Jamil S, et al. Advances and challenges of methanol-tolerant oxygen reduction reaction electrocatalysts for the direct methanol fuel cell. *J Energy Chem* 2023;77:499-513. DOI
18. Ma Z, Legrand U, Pahija E, Tavares JR, Boffito DC. From CO_2 to formic acid fuel cells. *Ind Eng Chem Res* 2021;60:803-15. DOI
19. Zhang Y, Li F, Dong J, Jia K, Sun T, Xu L. Recent advances in designing efficient electrocatalysts for electrochemical carbon dioxide reduction to formic acid/formate. *J Electroanal Chem* 2023;928:117018. DOI
20. Shi Y, Ma ZR, Xiao YY, et al. Electronic metal-support interaction modulates single-atom platinum catalysis for hydrogen evolution reaction. *Nat Commun* 2021;12:3021. DOI PubMed PMC
21. Shi Y, Lee C, Tan X, et al. Atomic-level metal electrodeposition: synthetic strategies, applications, and catalytic mechanism in electrochemical energy conversion. *Small Struct* 2022;3:2100185. DOI
22. Tryk DA, Kuzume A. The electrochemistry of platinum-group and noble metals as it relates to fuel cells and water electrolysis: vibrational spectroscopic and computational insights. *Curr Opin Electrochem* 2023;41:101372. DOI
23. Jeong H, Oh J, Yi GS, et al. High-performance water electrolyzer with minimum platinum group metal usage: iron nitride-iridium oxide core-shell nanostructures for stable and efficient oxygen evolution reaction. *Appl Catal B Environ* 2023;330:122596. DOI
24. Hou J, Yang M, Ke C, et al. Platinum-group-metal catalysts for proton exchange membrane fuel cells: from catalyst design to electrode structure optimization. *EnergyChem* 2020;2:100023. DOI
25. Seselj N, Alfaro SM, Bompolaki E, Cleemann LN, Torres T, Azizi K. Catalyst development for high-temperature polymer electrolyte membrane fuel cell (HT-PEMFC) applications. *Adv Mater* 2023;35:e2302207. DOI PubMed
26. Wang J, Zhang B, Guo W, et al. Toward electrocatalytic methanol oxidation reaction: longstanding debates and emerging catalysts. *Adv Mater* 2023;35:e2211099. DOI
27. Sun Y, Chen W, Zhang W, et al. Trimetallic porous PtIrBi nanoplates with robust CO tolerance for enhanced formic acid oxidation catalysis. *Adv Funct Mater* 2023;33:2303299. DOI
28. Kim H, Hong S, Kim H, Jun Y, Kim SY, Ahn SH. Recent progress in Pt-based electrocatalysts for ammonia oxidation reaction. *Appl*

Mater Today 2022;29:101640. DOI

29.   Lin HY, Lou ZX, Ding Y, et al. Oxygen evolution electrocatalysts for the proton exchange membrane electrolyzer: challenges on stability. *Small Methods* 2022;6:e2201130. DOI

30.   Ren X, Wang Y, Liu A, Zhang Z, Lv Q, Liu B. Current progress and performance improvement of Pt/C catalysts for fuel cells. *J Mater Chem A* 2020;8:24284-306. DOI

31.   Liu M, Zhao Z, Duan X, Huang Y. Nanoscale structure design for high-performance Pt-based ORR catalysts. *Adv Mater* 2019;31:1802234. DOI PubMed

32.   Hu S, Ge S, Liu H, Kang X, Yu Q, Liu B. Low-dimensional electrocatalysts for acidic oxygen evolution: intrinsic activity, high current density operation, and long-term stability. *Adv Funct Mater* 2022;32:2201726. DOI

33.   Ruban A, Hammer B, Stoltze P, Skriver H, Nørskov J. Surface electronic structure and reactivity of transition and noble metals. *J Mol Catal A Chem* 1997;115:421-9. DOI

34.   You B, Tang MT, Tsai C, Abild-Pedersen F, Zheng X, Li H. Enhancing electrocatalytic water splitting by strain engineering. *Adv Mater* 2019;31:e1807001. DOI

35.   Gawande MB, Goswami A, Asefa T, et al. Core-shell nanoparticles: synthesis and applications in catalysis and electrocatalysis. *Chem Soc Rev* 2015;44:7540-90. DOI

36.   Kunene T, Kwanda Tartibu L, Ukoba K, Jen T. Review of atomic layer deposition process, application and modeling tools. *Mater Today Proc* 2022;62:S95-109. DOI

37.   Vasilyev VY, Morozova NB, Basova TV, Igumenov IK, Hassan A. Chemical vapour deposition of Ir-based coatings: chemistry, processes and applications. *RSC Adv* 2015;5:32034-63. DOI

38.   Pandey PA, Bell GR, Rourke JP, et al. Physical vapor deposition of metal nanoparticles on chemically modified graphene: observations on metal-graphene interactions. *Small* 2011;7:3202-10. DOI

39.   Liang J, Liu Q, Li T, et al. Magnetron sputtering enabled sustainable synthesis of nanomaterials for energy electrocatalysis. *Green Chem* 2021;23:2834-67. DOI

40.   Kim J, Kim H, Han GH, et al. Electrodeposition: an efficient method to fabricate self-supported electrodes for electrochemical energy conversion systems. *Exploration* 2022;2:20210077. DOI PubMed PMC

41.   Yeo K, Eo J, Kim MJ, Kim S. Shape control of metal nanostructures by electrodeposition and their applications in electrocatalysis. *J Electrochem Soc* 2022;169:112502. DOI

42.   Kale MB, Borse RA, Mohamed AGA, Wang Y. Electrocatalysts by electrodeposition: recent advances, synthesis methods, and applications in energy conversion. *Adv Funct Mater* 2021;31:2101313. DOI

43.   Dimitrov N. Recent advances in the growth of metals, alloys, and multilayers by surface limited redox replacement (SLRR) based approaches. *Electrochim Acta* 2016;209:599-622. DOI

44.   Liu Y, Gokcen D, Bertocci U, Moffat TP. Self-terminating growth of platinum films by electrochemical deposition. *Science* 2012;338:1327-30. DOI PubMed

45.   Switzer JA. Atomic layer electrodeposition. *Science* 2012;338:1300-1. DOI PubMed

46.   Liu Y, Hangarter CM, Garcia D, Moffat TP. Self-terminating electrodeposition of ultrathin Pt films on Ni: an active, low-cost electrode for H_2 production. *Surf Sci* 2015;631:141-54. DOI

47.   Ahn SH, Liu Y, Moffat TP. Ultrathin platinum films for methanol and formic acid oxidation: activity as a function of film thickness and coverage. *ACS Catal* 2015;5:2124-36. DOI

48.   Ahn SH, Tan H, Haensch M, Liu Y, Bendersky LA, Moffat TP. Self-terminated electrodeposition of iridium electrocatalysts. *Energy Environ Sci* 2015;8:3557-62. DOI

49.   Liu Y, You H, Kimmel YC, Esposito DV, Chen JG, Moffat TP. Self-terminating electrodeposition of Pt on WC electrocatalysts. *Chem Mater* 2020;504:144472. DOI PubMed PMC

50.   Kim H, Kim J, Han GH, Jang HW, Kim SY, Ahn SH. Hydrogen evolving electrode with low Pt loading fabricated by repeated pulse electrodeposition. *Korean J Chem Eng* 2020;37:1340-5. DOI

51.   Kim H, Kim J, Kim J, et al. Dendritic gold-supported iridium/iridium oxide ultra-low loading electrodes for high-performance proton exchange membrane water electrolyzer. *Appl Catal B Environ* 2021;283:119596. DOI

52.   Hong S, Kim H, Kim J, Kim S, Ahn S. Electrochemical synthesis of Pt-decorated Au dendrite anode for constructing a direct formic acid fuel cell. *Mater Today Chem* 2022;26:101162. DOI

53.   Kim J, Kim H, Kim S, et al. Atomic Pt clusters on Au dendrite for formic acid oxidation. *Chem Eng J* 2023;451:138664. DOI

54.   Kim H, Choe S, Park H, Jang JH, Ahn SH, Kim SK. An extremely low Pt loading cathode for a highly efficient proton exchange membrane water electrolyzer. *Nanoscale* 2017;9:19045-9. DOI

55.   Kim D, Kim H, Park H, et al. Performance enhancement of high-temperature polymer electrolyte membrane fuel cells using Pt pulse electrodeposition. *J Power Sources* 2019;438:227022. DOI

56.   Byun J, Ahn SH, Kim JJ. Self-terminated electrodeposition of platinum on titanium nitride for methanol oxidation reaction in acidic electrolyte. *Int J Hydrog Energy* 2020;45:9603-11. DOI

57.   Li M, Ma Q, Zi W, Liu X, Zhu X, Liu SF. Pt monolayer coating on complex network substrate with high catalytic activity for the hydrogen evolution reaction. *Sci Adv* 2015;1:e1400268. DOI PubMed PMC

58.   Pang L, Li M, Ma Q, et al. Controlled Pt monolayer fabrication on complex carbon fiber structures for superior catalytic applications. *Electrochim Acta* 2016;222:1522-7. DOI

59. Pang L, Zhang Y, Liu SF. Monolayer-by-monolayer growth of platinum films on complex carbon fiber paper structure. *Appl Surf Sci* 2017;407:386-90. DOI

60. Kim D, Kim J. Effect of anionic electrolytes and precursor concentrations on the electrodeposited Pt structures. *Electroanalysis* 2017;29:387-91. DOI

61. Jeong H, Kim J. Insights into the electrooxidation mechanism of formic acid on Pt layers on Au examined by electrochemical SERS. *J Phys Chem C* 2016;120:24271-8. DOI

62. Lee E, Sung M, Wang Y, Kim J. Atomic layer electrodeposition of Pt on nanoporous Au and its application in pH sensing. *Electroanalysis* 2018;30:2028-34. DOI

63. Jeong H, Kim J. Methanol dehydrogenation reaction at Au@Pt catalysts: insight into the methanol electrooxidation. *Electrochim Acta* 2018;283:11-7. DOI

64. Wang Y, Kim J. Oxygen evolution reaction on nanoporous gold modified with Ir and Pt: synergistic electrocatalysis between structure and composition. *Electroanalysis* 2019;31:1026-33. DOI

65. Elezović N, Branković G, Zabinski P, Marzec M, Jović V. Ultra-thin layers of iridium electrodeposited on Ti$_2$AlC support as cost effective catalysts for hydrogen production by water electrolysis. *J Electroanal Chem* 2020;878:114575. DOI

66. Elezović N, Krstajić-pajić M, Jović V. Sub-monolayers of iridium electrodeposited on Ti$_2$AlC substrate as catalysts for hydrogen evolution reaction in sulfuric acid solution. *Zaštita Materijala* 2020;61:181-91. DOI

67. Elezović NR, Zabinski P, Lačnjevac UČ, Pajić MNK, Jović VD. Electrochemical deposition and characterization of iridium oxide films on Ti$_2$AlC support for oxygen evolution reaction. *J Solid State Electrochem* 2021;25:351-63. DOI

68. Petričević A, Jović V, Krstajić-pajić M, Zabinski P, Elezović N. Oxygen reduction reaction on electrochemically deposited sub-monolayers and ultra-thin layers of Pt on (Nb-Ti)$_2$AlC substrate. *Zaštita Materijala* 2022;63:153-64. DOI

69. Deng Y, Tripkovic V, Rossmeisl J, Arenz M. Oxygen reduction reaction on Pt overlayers deposited onto a gold film: ligand, strain, and ensemble effect. *ACS Catal* 2016;6:671-6. DOI

70. Lapp AS, Duan Z, Marcella N, et al. Experimental and theoretical structural investigation of AuPt nanoparticles synthesized using a direct electrochemical method. *J Am Chem Soc* 2018;140:6249-59. DOI

71. Proch S, Yoshino S, Kitazumi K, Seki J, Kodama K, Morimoto Y. Over-potential deposited hydrogen (Hopd) as terminating agent for platinum and gold electro(co)deposition. *Electrocatalysis* 2019;10:591-603. DOI

72. Lapp AS, Crooks RM. Multilayer electrodeposition of Pt onto 1-2 nm Au nanoparticles using a hydride-termination approach. *Nanoscale* 2020;12:11026-39. DOI PubMed

73. Pfisterer JHK, Liang Y, Schneider O, Bandarenka AS. Direct instrumental identification of catalytically active surface sites. *Nature* 2017;549:74-7. DOI PubMed

74. Chang JC, Garner CS. Kinetics of aquation of aquopentachloroiridate(III) and chloride anation of diaquotetrachloroiridate(III) anions. *Inorg Chem* 1965;4:209-15. DOI

75. Poulsen IA, Garner CS. A thermodynamic and kinetic study of hexachloro and aquopentachloro complexes of iridium(III) in aqueous solutions. *J Am Chem Soc* 1962;84:2032-7. DOI

76. Ahn M, Kim J. Insights into the electrooxidation of formic acid on Pt and Pd shells on Au core surfaces via SERS at dendritic Au rod electrodes. *J Phys Chem C* 2013;117:24438-45. DOI

77. Hyun M, Choi S, Lee YW, Kwon SH, Han SW, Kim J. Simple electrodeposition of dendritic Au rods from sulfite-based Au(I) electrolytes with high electrocatalytic and SERS activities. *Electroanalysis* 2011;23:2030-5. DOI

78. Choi S, Ahn M, Kim J. Highly reproducible surface-enhanced Raman scattering-active Au nanostructures prepared by simple electrodeposition: origin of surface-enhanced Raman scattering activity and applications as electrochemical substrates. *Anal Chim Acta* 2013;779:1-7. DOI

79. Cao D, Lu GQ, Wieckowski A, Wasileski SA, Neurock M. Mechanisms of methanol decomposition on platinum: a combined experimental and ab initio approach. *J Phys Chem B* 2005;109:11622-33. DOI PubMed

80. Musthafa OT, Sampath S. High performance platinized titanium nitride catalyst for methanol oxidation. *Chem Commun* 2008;67-9. DOI PubMed

81. Marković NM, Sarraf ST, Gasteiger HA, Ross PN. Hydrogen electrochemistry on platinum low-index single-crystal surfaces in alkaline solution. *J Chem Soc Faraday Trans* 1996;92:3719-25. DOI

82. Subbaraman R, Tripkovic D, Strmcnik D, et al. Enhancing hydrogen evolution activity in water splitting by tailoring Li$^+$-Ni(OH)$_2$-Pt interfaces. *Science* 2011;334:1256-60. DOI

83. Danilovic N, Subbaraman R, Chang KC, et al. Activity-stability trends for the oxygen evolution reaction on monometallic oxides in acidic environments. *J Phys Chem Lett* 2014;5:2474-8. DOI

84. Cherevko S, Geiger S, Kasian O, et al. Oxygen and hydrogen evolution reactions on Ru, RuO$_2$, Ir, and IrO$_2$ thin film electrodes in acidic and alkaline electrolytes: a comparative study on activity and stability. *Catal Today* 2016;262:170-80. DOI

85. Kasian O, Grote JP, Geiger S, Cherevko S, Mayrhofer KJJ. The common intermediates of oxygen evolution and dissolution reactions during water electrolysis on iridium. *Angew Chem Int Ed* 2018;57:2488-91. DOI PubMed PMC

86. Rao C, Cabrera CR, Ishikawa Y. Graphene-supported Pt-Au alloy nanoparticles: a highly efficient anode for direct formic acid fuel cells. *J Phys Chem C* 2011;115:21963-70. DOI

87. Kong F, Du C, Ye J, Chen G, Du L, Yin G. Selective surface engineering of heterogeneous nanostructures: in situ unraveling of the catalytic mechanism on Pt-Au catalyst. *ACS Catal* 2017;7:7923-9. DOI

88. Duchesne PN, Li ZY, Deming CP, et al. Golden single-atomic-site platinum electrocatalysts. *Nat Mater* 2018;17:1033-9. DOI

89. Zhong W, Qi Y, Deng M. The ensemble effect of formic acid oxidation on platinum-gold electrode studied by first-principles calculations. *J Power Sources* 2015;278:203-12. DOI

90. Avasarala B, Haldar P. Electrochemical oxidation behavior of titanium nitride based electrocatalysts under PEM fuel cell conditions. *Electrochim Acta* 2010;55:9024-34. DOI

91. Zhang RQ, Lee TH, Yu BD, Stampfl C, Soon A. The role of titanium nitride supports for single-atom platinum-based catalysts in fuel cell technology. *Phys Chem Chem Phys* 2012;14:16552-7. DOI PubMed

92. Grozovski V, Climent V, Herrero E, Feliu JM. Intrinsic activity and poisoning rate for HCOOH oxidation at Pt(100) and vicinal surfaces containing monoatomic (111) steps. *Chemphyschem* 2009;10:1922-6. DOI